UNIVERSITÀ DEL SALENTO

FACOLTÀ DI SCIENZE MM. FF. NN.

Dott. Giuseppina Terracciano
PhD Thesis

Charged particles tracking at the International Linear Collider

Supervisors:
Dott. Francesco Grancagnolo
Dott. Corrado Gatto

Coordinatore:
Chiar.mo Prof.Gilberto Leggieri

Dottorato di ricerca in Fisica XXI ciclo

Contents

List of Figures

List of Tables

Introduction

In the last century elementary particles physics has made a significant step forward with the development of the Standard Model. Experiments have determined the particle constituents of ordinary matter and identified four types of forces binding matter. This success has led particle physicist to address even more fundamental questions and to explore deeper mysteries in science. The International Linear Collider is expected to play a central role in exploring a new scientific landscape. In fact, amoung the major physics goals of the ILC are the understanding of the mechanism behind mass generation and electroweak symmetry breaking, the searching for and, perhaps, the discovering of supersymmetric particles and the confirmation of their supersymmetric nature and the hunting for signs of extra space time dimension and ofquantum gravity. In addition, making precision measurements of standard model processes will open windows on physics at energy scales beyond a direct reach.

The physics under study at ILC requires a detector with capabilities far beyond those of the detectors at LEP or LHC. The ILC machine environment, calls for detector designs of much higher performance than the detectors planned for the LHC, with much better jet energy resolution, tracker momentum resolution, and vertex detector impact parameter resolution.Three ILC detector concepts have emerged in the last few year, the International

Large Detector (ILD), the Silicon Detector (SiD) and the 4^{th} Concept.

This thesis describes the most innovative proposal for a detector at the ILC, the 4^{th} Concept. This concept differs from the other two concepts in several respects. The 4^{th} Concept adopted a novel implementation of a dual-readout compensating calorimetry, a low mass, cluster-timing drift chamber (CluCou, KLOE-style) for a precise reconstruction of tracks in space and a iron free dual-solenoid muon system with drift tubes for the precise measurement of bending of muons in air to achieve high acceptance and a good muon momentum resolution. Detailed descriptions of the 4th Detector tracking subsystems, Drift Chamber and Muon spectrometer are presented. Finally, thanks to of these detectors the unprecedented precision, the analysis of one particlular process, the Higgs breemsstrahlung, i.e., $e^+e^- \rightarrow ZH$, with $Z \rightarrow \mu^+\mu^-$ or e^+e^- is presented.

The thesis is structured in four chapters. The first chapter contains a short summary of the Standard Model theory, with a brief an introduction to the Physics beyond the Standard Model and a description of possible physics results at ILC. In the second chapter a review of the main characteristics of three ILC detector concepts that have emerged in the last few year, is presented. In the same chapter a brief description of the ILCRoot software, a tool for full simulation and analysis of theevents at ILC is presented. The third chapter contains a detailed description of the main tracking subsystems of the 4^{th} Detector and their performances. Finally, the last chapter describes in detail the physics analysis of the Higgs breemsstrahlung production process, with the identification of the Z in pairs of charged leptons.

Chapter 1

Physics reach at the International Linear Collider

1.1 Introduction

The physics of elementary particles and of their interactions has played a key role in the evolution of the Universe from the big bang to its present appearance in terms of galaxies, stars, black holes, chemical elements and biological systems. The past century has been characterized by an enormous progress towards an understanding of the innermost secrets of the Universe. The results obtained in particle physics have revealed a complex microphysical world, which however seems to obey simple mathematical descriptions, governed by symmetry principles. In our current understanding of the nature there are four fundamental forces, strong, electromagnetic, weak and gravity, where electromagnetic and weak interactions have been found to emerge from the unified electroweak interactions. So far, we have been able to formulate a quantum theory of elementary particles based on the strong and electroweak interactions. The quantum nature of the interactions means that they arise from the interchange of particles, namely the massless photon, massive W and Z bosons for the electroweak interactions, and the massless gluon for the strong interaction. According to current understanding, there seems to be indications pointing towards a unification of the strong and electroweak forces, and it appears to be conceivable that also gravity, with the graviton as mediator of the interaction, may be incorporated into the unified framework. However, we know that our picture of the observed forces and particle is incomplete. There needs to be another ingredient, being related to the origin of mass and the breaking of the symmetry governing the electroweak interaction (EWSB). Such ingredient is probably a Higgs field, a scalar field that spreads out over the whole space. Its quantum field is the Higgs particle. If no fundamental Higgs boson exits in nature, electroweak symmetry breaking can still occur, for instance, via a new kind of strong interaction. The Higgs boson is the last missing ingredient of the “standard model”(SM) of particle physics.

There are indications that new physics beyond the SM should manifest itself below an energy scale of about 1 TeV. A particular shortcoming of the SM is its instability against the huge hierarchy of vastly different scales relevant in particle physics, in particular the electroweak scale at a few GeV and Planck scale at about 10^{19} GeV, where the strengths of gravity and the other interactions become comparable. Moreover there is clear evidence for a “cold Dark Matter”, for which the SM does not offer an explanation. The known properties of Dark Matter could arise in particular if new weakly massive particles exist, which requires an extension of the SM.

A possibility of new physics that stabilizes the hierarchy between the electroweak and the Plack scale is supersymmetry (SUSY), i.e. the extension of space and time by new supersymmetric coordinates. Other ideas to solve the hierarchy problem postulate extra spatial dimensions beyond the three that we observe in our evey-day life, or new particles at the several TeV scale. Susy has also a direct explanation for Dark Matter through a number of new particles that can be the source of that.

In this chapter I make a brief description of The Standard Model and of some scenarios of new physics beyond the Standard Model. I also describe how lepton linear collider whose energy is beyond the current reach of accelerators, could be the appropriate tool to unravel many of the possible extensions to the SM.

1.2 Overview of The Standard Model

The Standard Model (SM) of fundamental interactions describes the matter as composed by half-integer spin particles, the *fermions*, that can be divided in two main groups: *leptons*, including electrons, muons, taus and neutrinos, and *quarks*. The latter have fractional charge and do not freely exit in nature; they are the constituents of a wide class of particles, the *hadrons*.

Interactions between particles are described in terms of the exchange of *bosons*, integer spin particles that mediate fundamental interactions. The bond between atoms and molecules is due to the *electromagnetic interaction*, while the weak interaction explains, for example, nuclear β-decays. Finally, the strong interaction is responsible for the confinement of quarks inside hadrons.

The Standard Model describes these interactions with two gauge theories:

- Glashow–Salam–Weinberg electroweak theory that unifies the electromagnetic and weak interactions [1];

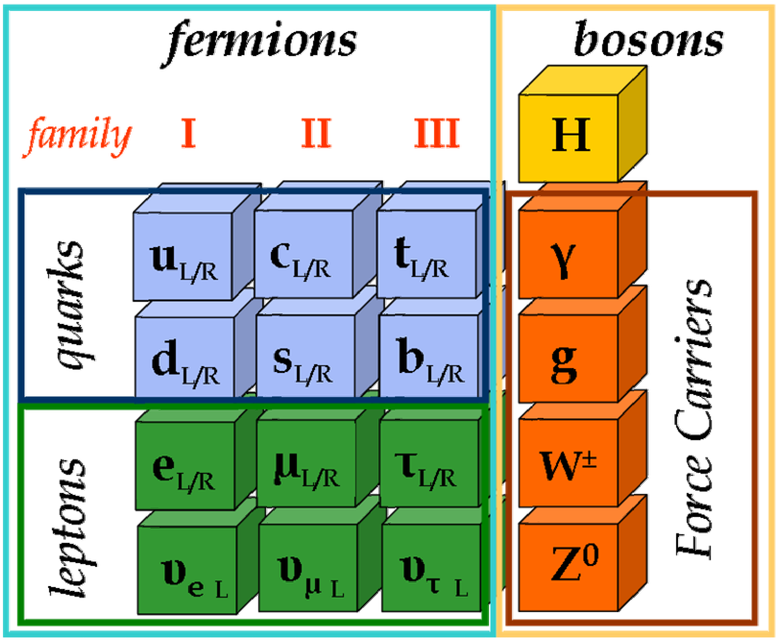

Figure 1.1: *Standard Model particles.*

- the theory of strong interaction or Quantum Chromo Dynamics(QCD) that describes the strong interactions between quarks and gluons [2].

1.2.1 EWSB and Higgs mechanism

The theory of electromagnetic interaction is called Quantum Electro-Dynamics (QED), and it is based on the invariance of the Lagrangian for local gauge transformations with respect to the $U(1)$ symmetry group. This condition leads to the existence of a massless vector field, the photon (γ).

The unification of the theory of electromagnetism and that of weak interactions is accomplished by extending the symmetry to the group $SU(2) \times U(1)$[3], which is associated to the quantum numbers I (*weak isospin*) and

Y (*hypercharge*), that satisfy the relation:

$$Q = I_3 + \frac{Y}{2} \tag{1.1}$$

where I_3 is the third component of the weak isospin and Q is the electric charge.

The invariance for local gauge transformations with respect to the $SU(2) \times U(1)$ group introduces four massless vector field, $W_\mu^{1,2,3}$ and B_μ, that couple to fermions with two coupling constants, g and *g'*. The corresponding physical fields are linear combination of $W_\mu^{1,2,3}$ and B_μ: the charged bosons W^+ and W^- correspond to

$$W_\mu^\pm = \sqrt{\frac{1}{2}}(W_\mu^1 \pm i W_\mu^2) \tag{1.2}$$

while the neutral bosons γ and Z correspond to

$$A_\mu = B_\mu \cos\theta_W + W_\mu^3 \sin\theta_W \tag{1.3}$$

$$Z_\mu = -B_\mu \sin\theta_W + W_\mu^3 \cos\theta_W \tag{1.4}$$

obtained by mixing the neutral fields W_μ^3 and B_μ with a rotation defined by the $Weinberg\ angle\ \theta_W$. The field A_μ is identified with the tensor of the electromagnetic field. By requiring the coupling terms to be equal, one obtains:

$$g \sin\theta_W = g' \cos\theta_W = e \tag{1.5}$$

that represents the electroweak unification.

Up to this point, all particles are massless: in the $SU(2) \times U(1)$ Lagrangian, a mass term for the gauge bosons would violate gauge invariance. Masses are introduced with the *Higgs mechanism*, that allows fermions and $W^\pm$ and Z bosons to be massive, while keeping the photon massless. This is accomplished by introducing the *Higgs field*, a $SU(2)$ doublet of the complex scalar field:

$$\phi = \begin{pmatrix} \phi^+ \\ \phi^0 \end{pmatrix} = \begin{pmatrix} \frac{1}{\sqrt{2}}\left(\phi_1 + i\phi_2\right) \\ \frac{1}{\sqrt{2}}\left(\phi_3 + i\phi_4\right) \end{pmatrix} \tag{1.6}$$

The Lagrangian of this field must be invariant under $SU(2) \times U(1)$ local gauge transformations and includes a potential term

$$V(\phi) = -\mu^2 \phi^\dagger \phi + \lambda \left(\phi^\dagger \phi\right)^2 \tag{1.7}$$

where $\mu^2 \ > 0$ and $\lambda \ > 0$, so that the potential has a minimum for

$$\phi^\dagger \phi^+ = \frac{1}{2}(\phi_1^2 + \phi_2^2 + \phi_3^2 + \phi_4^2) = \frac{\mu^2}{2\lambda} = \frac{v^2}{2} \tag{1.8}$$

One is free to choose the values of $\phi_i = 0$ that respects this condition. The fact that minimum is not found for $\phi_i = 0$ but for a manifold of values, is called *spontaneous symmetry breaking* .

Boson masses derive from the coupling of the boson fields with non-zero vacuum value of the Higgs field: the potential in its fundamental state do not have the symmetry properties of the Lagrangian. However, it can be shown that the minimum for Higgs field is invariant for $U(1)$ transformations[3]. The electromagnetic $U(1)$ symmetry is unbroken and the photon remains massless.

The Higgs mechanism gives rise to three massive gauge bosons, corresponding to nine degrees of freedom. Since the initial number of independent fields is ten (three massless bosons with two polarisations states each, plus the four real ϕ_i fields), one additional scalar gauge boson should appear as a real particle. This is the *Higgs boson.* The Higgs mass is predicted to be:

$$m_H = \sqrt{2\lambda} v$$

This mass depend on v and λ, and the value v is related to the boson mass by relation:

$$m_W = \frac{vg}{2} \qquad m_Z = \frac{gv}{2\cos\theta_W}$$

The value of v (246 GeV) is known through its relation to the Fermi coupling costant G_F ($v = (\sqrt{2}G_F)^{\frac{-1}{2}}$) which is obtained with high precision from muon decay measurements. The parameter λ is characteristic of the field ϕ and is unknown. It remains a free parameter of the theory, therefore, the Higgs mass is unknown.

The fermion masses are generated with a similar mechanism, but appear as free parameters of the theory, six for the quarks and three for leptons (assuming neutrinos to be massless). These bring the number of parameters of the SM from three to 17, the others being the four independent elements of the Cabibbo-Kobayashi-Maskawa matrix that describes the mixing of quark flavours, the couplings g and g', the parameter v of the Higgs vacuum expectation value and Higgs mass.

All these parameters, except for the mass of the Higgs boson which has not yet been observed, can be determinated from experimental observations. The measurements of these quantities allow therefore for a consistency check of the electroweak Standard Model, which up to now has been confirmed with very high accuracy.

Higgs Boson Mass Bounds

The mass m_H of the Higgs boson is not predicted by the SM but constraints on its value can be obtained from theoretical and experimental considerations.

The Higgs potential of Eq.1.7 is affected by radiative corrections, which involve the mass of bosons and fermions and depends on the renormalisation

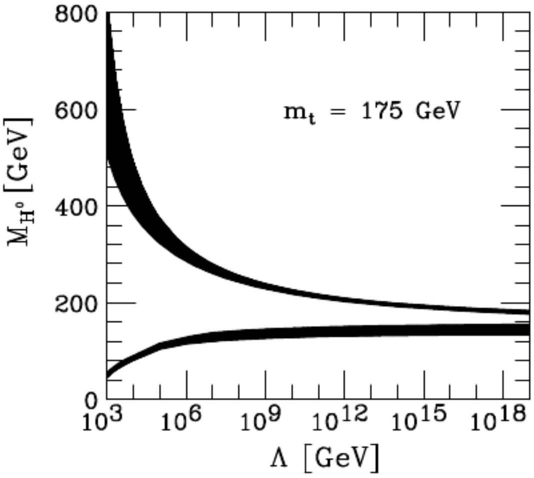

Figure 1.2: *Theoretical bounds on the Higgs mass as a function of the energy scale Λ up to which the Standard Model is valid [3]*

scale Λ. Radiative corrections might change the shape of the potential so that it has no absolute minimum. The request of *vacuum stability*, *i.e.* that the λ coefficient is large enough to avoid instability up to a certain scale Λ, implies a lower bound on the Higgs mass. On the other hand, due to running of the coupling, λ increases with the energy scale. The request that it remains finite up to a scale Λ(*triviality*) corresponds to an upper bound on m_H.

In both cases, the parameter Λ represents the scale up to which the SM is assumed to be valid. The theoretical bounds on m_H as a function of Λ are shown in Fig.1.2 For the SM to remain valid up to the Planck scale ($\Lambda = 10^{19}$ GeV), the Higgs mass must be in the range 130-200 GeV/c^2. Assuming the SM to be valid only up $\Lambda \sim 1$ TeV, the Higgs mass can be up to 700 GeV/c^2. In any case, new colliders should search for the Higgs boson up to masses of order of ≈ 1 TeV.

Experimental bounds on m_H are provided by measurements at LEP, SLC,

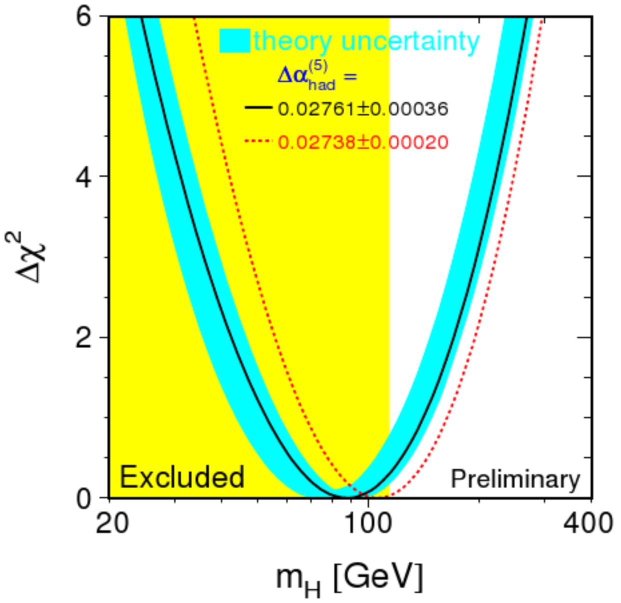

Figure 1.3: $\Delta\chi^2$ *of the fit electrweak measurements of LEP, SLC and tevatron as a function of the he Higgs mass [4]*

and Tevatron [4]. Direct searches excluded the region below 114.4 GeV/c^2 at 95% confidence level. Precision electroweak measurements are logarithmically sensitive to the Higgs mass due to radiative corrections. Electroweak data can therefore be fitted taking m_H as free parameter. In Fig 1.3 the shape of the χ^2 of the fit is shown as a function of m_H. The curve is shallow and the minimum is below the value excluded by direct searches (shaded area). One may conclude nevertheless that the fit privileges low values of the Higgs mass. An upper limit of 170 GeV/c^2 can be set at 95% confidence level.

1.2.2 Quantum-Cromo-Dynamics

Quantum Chromodynamics (QCD) is a gauge theory designed to model the strong interactions. It is based on the SU(3) group, which is a symmetry leading to the conservation of a quantity (or quantum number, or charge) called *colour*. The only elementary particles which interact strongly are the *quarks* and the *antiquarks*, via colour carrying gluons which represent the $3^2 - 1 = 8$ generators of the SU(3) group. The colours are labelled *red*, *green* and *blue* for the quarks, and *antired*, *antigreen* and *antiblue* for the antiquarks. QCD has two peculiar properties, called $asymptotic freedom$ and $confinement$. Asymptotic freedom means that in very high-energy interactions, the quarks and the gluons interact weakly. This behaviour was predicted from QCD in the early 1970s by D. Politzer, F. Wilczek and D. Gross [[5],[6]]. Confinement, on the other hand, means that the force between quarks does not diminish as they are separated. Because of this, it would take an infinite amount of energy to separate two quarks. Therefore they are forever bound into neutral colour hadrons such as the proton and the neutron, which also explains the consistent failure of free quark searches. A neutral colour state, or colour singlet, can be obtained by adding all three colours, all three anticolours or a colour charge and the equivalent anticolour charge. Hadrons can therefore be of two types: *(anti)baryons* consisting of three (anti)quarks, each of a different *(anti)colour*, or *mesons* consisting of a quark of a certain colour and an antiquark which carries the corresponding anticolour. The proton and antiproton are examples of baryons. They consist of two u quarks and one d quark or two $anti - u$ quarks and one $anti - d$ quark, respectively. These are called valence quarks, and they interact with each other via the exchange of gluons, which in turn can split into quark-antiquark pairs or emit more gluons, forming a sea of quarks and gluons. Since the asymptotic freedom means that the strong force decreases in strength as the energy scale of the interaction increases, a proton or an antiproton probed at high energy will consist of approximately non-interacting quarks and gluons (collectively called partons). Confinement makes QCD calculations of hadronic cross sections at low energy very complicated, due to the fact that bound states exist and perturbation series in the coupling constant cannot be applied. The calculations of QCD related quantities are therefore split in two parts in accordance to the factorisation theorem, separated in energy by the factorisation scale, F . The low-energy part is described using Parton Distribution Functions (PDFs), which give the momentum distribution of the constituent quarks and gluons. The PDFs are universal and process independent, being determined from fits to data using many different processes studied in many different experiments. Although PDFs cannot be derived from first principles, their evolution as a function of F is predictable in perturbation theory. At high energies, where the quarks and gluons can be considered free due to the weaker coupling of the strong force, the interactions can be approximated by perturbation series. Eventually, the free quarks and gluons hadronize, resulting in colourless bound states which can be identified as jets in the detector. At the moment, the exact process through which this happens is not fully understood, but several promising models exist.

1.3 Beyond the Standard Model

Even if up to now the SM has been experimentally confirmed with very high accuracy, the Higg boson has never been observed and it has been excluded by direct searches up to energies accessible at LEP.

Particles		SUSY partner	
Particle	Spin	Particle	Spin
quark (q)	$\frac{1}{2}$	squark ($\tilde{q}$)	0
lepton (l)	$\frac{1}{2}$	slepton ($\tilde{l}$)	0
gluon (G)	1	gluino ($\tilde{G}$)	$\frac{1}{2}$
$W^{\pm}$, Z^0, γ	1	chargino ($\tilde{\chi}^{\pm}_i \quad i = 1, 2$)	$\frac{1}{2}$
Higgs boson ($h, \ H, \ A, \ H^{\pm}$)	0	neutralino ($\tilde{\chi}^{0}_i \quad i = 1, 2, 3, 4$)	$\frac{1}{2}$

Table 1.1: *MSSM Particles.*

There are also several reasons to think that the SM is only an effective description and that a more fundamental theory must exit. We already observed that theoretical bounds on the Higgs mass can be derived from the request that, once radiative correction are included, the theory remains valid up to a certain energy scale. It is natural to think that at higher energy scales some general theory should be valid, possibly describing all interactions. In the SM, the strong interaction is described by a $SU(3)$ colour symmetry group, which however is not unified with the electroweak description. Gravity, whose strength should become comparable with that of the other interactions at the Planck scale (10^{19} GeV), is not included at all. It would be appealing to find a wider symmetry that describes all interactions and the reason why it is broken at lower energy scales. In addition, the Higgs mass suffers from divergences caused by radiative corrections which are proportional to the energy cutoff. For the SM to be valid up to very high energy scales, extremely precise cancellations should be present at all perturbations levels. Such cancellations are formally possible, but there is no reason why such a fine tuning should occur (*naturalness problem*).

Other considerations of more aesthetic nature are that the Higgs is an *ad* *hoc* addition to the SM, moreover it is the only scalar particle in the theory. Also, there is no explanation for the fact that the particle masses would be significantly smaller than the energy scale up to which the theory remains valid (*hierarchy problem*). Finally, the number of free parameters of the SM (17, neglecting neutrino masses and mixings) appears too high to be natural. Several solution for these problems have been proposed. Among them, supersymmetry (SUSY) is an elegant theory that introduces a new symmetry between boson and fermions. SUSY predicts that each particle has a supersymmetric partner whose spin differs by one half. The naturaless problem is solved by the fact that the loop contributions from particles and their supersymmetric parterns cancel. The simplest supersymmetric model, called the Minimal Supersymmetric Standard Model (MSSM) [7], requires at least two Higgs doublets, corresponding to five Higgs particles: two charged boson $H^{\pm}$, two scalar boson, h and H and one pseudo scalar, A. The MSSM predicts a rich phenomenology to appear below energies of about 1 TeV. However no evidence for supersymmetry has been observed yet.

1.4 The International Linear Collider

An e^+e^- linear collider in the energy range 0.5 - 1 TeV will be essential to make precise measurements in the region of electroweak symmetry-breaking which will be opened up by the Large Hadron Collider(LHC). This implies new requirement from theory and unprecedented experimental accuracies. This in turn drives the need for more precise theoretical responding effort for standard, Higgs and supersymmetry processes at the Terascale. There must be a corresponding effort to eliminate all known instrumental limitation which could compromise the precision of the measurements (limits on

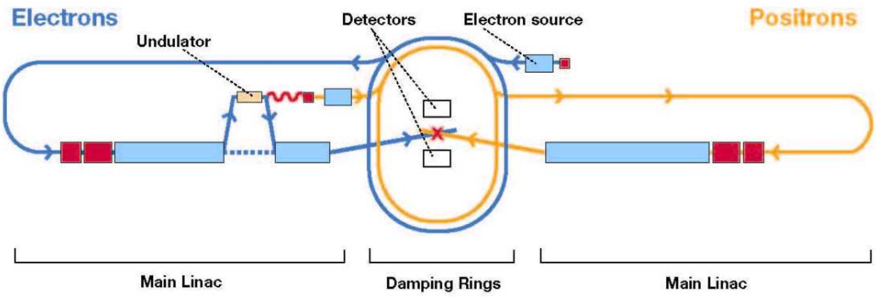

Figure 1.4: *Scheme of the ILC machines*

the accuracy of momentum resolution, jet reconstruction, reconstruction of short lived particles).

The e^+e^- linear collider will search for invisible particles, candidates of Dark Matter. This requires that the detector be as hermetic as possible. Machine backgrounds must be well controlled to reach the highest precision. The luminosity and polarisation of the beam must be also accurately known. Different proposals have been made for Linear Collider e^+e^- machines, NLC [8], JLC [9] and TESLA [10] in the past years. They have all converged into the International Linear Collider project (ILC). The accelerator has been designed to meet the basic parameters required for the planned physics program [11]. All of the physics scenarios considered indicate that a $\sqrt{s} = 500$ Gev collider can have a great impact on understanding the physics of the Terascale. An energy upgrade up to a $\sqrt{s} \sim 1$ TeV opens the door to even greater discoveries. With modest modifications, the ILC can also offer other options, although these are not included in the baseline design. The total luminosity required is 500 fb^{-1} within the first four years of operation and 1000 fb^{-1} during the first phase of operation at 500 GeV. The electron beam must have a polarisation larger than 80%. The positron source should be upgradable to produce a beam with more than ±50% polarisation[11]. Beam energy and polarisation must be stable and measurable at a level of about 0.1%.

The ILC is based on 1.3 GHz superconducting radio-frequency(SCRF) accelerating cavities. The cavities must be operated at 2° K to achieve their performance. The current ILC baseline assumes an average accelerating gradient of 31.5 MeV/m in the cavities to archieve a center of mass energy of 500 GeV and a peak luminosity of 2x10$^{34}cm^{-2}s^{-1}$. The high luminosity requires the use of high power and small beam. Figure 1.4 shows a schematic view of the overall layout of the ILC, indicating the location of the major subsystem. The total footprint is $\sim$ 31 Km. The electron source, the damping rings and the positron source are centrally located around the interaction region (IR). To upgrade the machine to E_{cms}= 1 TeV, the linacs and the beam transport lines from the damping rings would be extended by another $\sim$ 11 Km each.

1.4.1 Potential Physics Studies at the International Linear Collider

As mentioned in Sec. 1.4, the International Linear Collider(ILC) is foreseen to reach a centre of mass energy of up to 500 GeV with an upgrade to the TeV scale. Within its range, the study of several processes will be possible as shown in Fig 1.5. The ILC is referred to as a high precision machine as it is designed to provide high accuracy measurements mainly due a clean experimental environment. As an example, Tab.1.2 illustrates the current and anticipated future experimental uncertainties for the mass measurements of the W, the top and the indirect precision on the Higgs boson mass. If a Higgs boson exists within the TeV range, the ILC will be able to measure the full set of its properties with high precision. The observables on the Higgs, i.e.

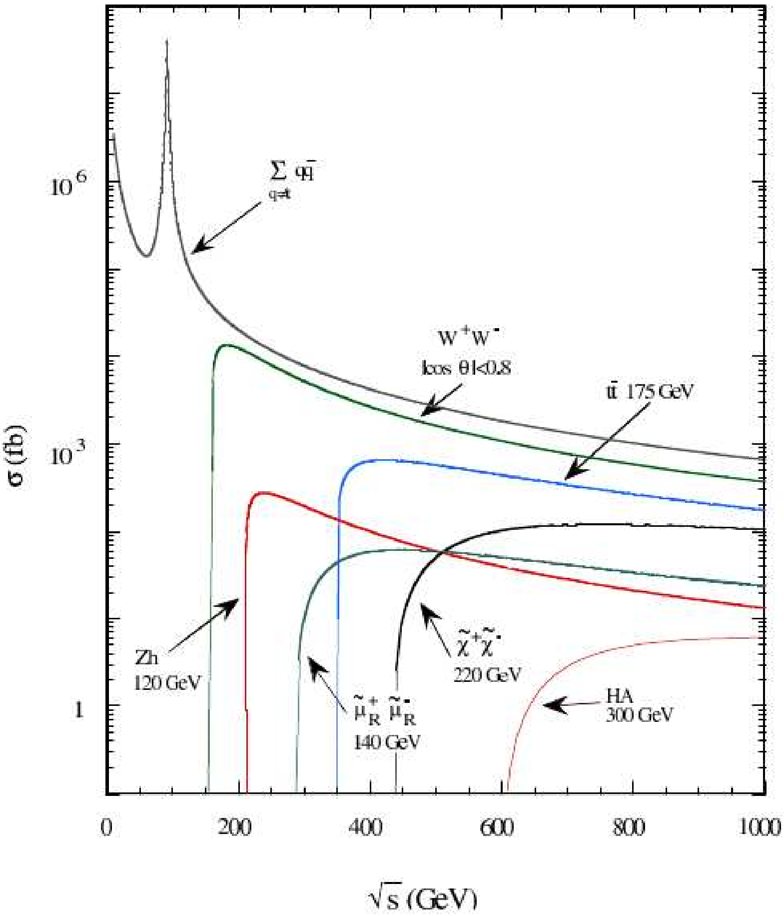

Figure 1.5: *cross-section for same intersting process at ILC* [12]

its mass, spin, and lifetime, its production cross section and branching ratios will decide if it has the profile predicted by the SM. Further studies to refine the existing precision can then constrain the model or reveal its origin from a supersymmetric world or other possible scenarios.

Supersymmetry illustrates the possible interplay between different experiments and observations. Missing energy signatured at the LHC may indicate a weakly interacting massive particle consistent with a supersymmetric particle. Direct or indirect dark matter searches may provide a signal for weakly

	now	LHC	ILC
$\delta M_W[MeV]$	33	15	10
$\delta m_t[GeV]$	5.1	1.0	0.2-0.1
$\delta m_h[MeV]$	-	100	50

Table 1.2: *the current and anticipated future experimental uncertainties for the mass measurements of the W, the top and the indirect precision on the Higgs boson mass.*

interacting exotic particles in our galactic halo. Are these particles neutralinos, responsible for some or all of the dark matter? ILC measurements will be mandatory for this analysis.

Alternative possible structures of the new physics include phenomena containing extra dimensions, introducing connections between Terascale physics and gravity. One possibility is that the weakness of gravity could be understood by the escape of the gravitons into the new large extra dimensions. Events with unbalanced momentum caused by the escaping gravitons could be seen by both the LHC and the ILC. The ILC could confirm this scenario by observing anomalous electron positron pair production caused by graviton exchange.

Chapter 2

The 4^{th} Concept at the ILC

2.1 Introduction

The physics topic under study at the ILC require detectors with capabilities far beyond these at LEP or LHC. The ILC machine environment permits detector designs of much higher performance than the detectors planned for the LHC, with superior jet energy, track momentum, and vertex impact parameter resolutions. This increased performance is needed at the ILC, for precision measurements of masses and branching fractions, final states identifiecation, low cross-section signals, new phenomena, and for exploiting the delivered luminosity as much as possible. Detector research and development is needed to reach these goals. Three ILC detector concepts have emerged in the last few year, the International Large Detector (ILD), the Silicon Detector (SiD) and the 4^{th} Concept. In this chapter, a brief review of the main characteristics of each concept are given. More details can be found in the respective Letter of Intent[13, 14, 15].

2.2 Detectors Concepts at ILC

The proposed detectors at ILC are characterized by

- excellent jet-energy resolution;
- good jet-flavor identication capability;
- excellent charged-particle momentum resolution;
- hermetic calorimeter coverage.

Two of the concepts (ILD and SiD) use magnetic flux return iron yoke for their traditional solenoidal magnetic fields and adopt the particle flow calorimetry strategy (PFA), with highly segmented electromagnetic and hadronic calorimeters for the separation of the energy deposited by charged tracks, photons and neutral hadrons. The 4^{th} Concept adopts, instead, a muon system in air, thanks to a dual-solenoid magnetic field configuration, stresses excellent muon momentum resolution, and utilizes a novel dual readout calorimeter scheme. All three concepts employ similar pixellated vertex detectors, which provide high precision vertex reconstruction and have sophisticated tracking systems which have been optimized for high track reconstruction efficiency and excellent momentum resolution. The performance goal for the detector systems are:

- jet energy resolution of $\Delta E_j/E_j \leq 30\%/\sqrt{E_j(GeV)}$;
- impact parameter resolution of $\sigma_b \leq 5 \oplus \dfrac{10}{p\beta \sin^{3/2}\Theta}$ (μm) for jet flavor tagging;
- transverse momentum resolution of $\delta p_t/p_t^2 \leq 2x10^{-5} \oplus 1 \cdot 10^{-3}$ $(GeV/c)^{-1}$ for charged track;
- hermeticity down to 5 mrad around the beam line.

2.2.1 ILD Concept

In ILD (International Large Detector) excellent calorimetry and tracking are combined to obtain the best possible overall event reconstruction, by identifying individual particles within jets for particle flow analysis. This requires excellent granularity for all detector systems. The main features of ILD are outlined below.

A Si-pixel based vertex detector (VXT) enables long lived particles such as $b - hadrons$ and $c - hadrons$ to be reconstructed.

The central component of the ILD tracker is a Time Projection Chamber (TPC) which provides up to 224 precise measurements along the track of a charged particle. This is supplemented by a system of Silicon (Si) based Tracking detectors, which provide additional measurements points downstream and upstreams of the TPC, and extend the angular coverage down to very small angle.

This combination of tracking devices result in high track reconstruction efficiencies and good momentum resolution.

The particle flow calorimetry is used for measuring the jet-energy. Excellent jet energy resolution is achieved when every particle in the event, charged and neutral, is measured with the best possible precision. This goal is achieved by reconstructing charged particles in the tracking, photons in the electromagnetic calorimeter (ECAL), and neutral hadrons in both the ECAL and the hadronic calorimeter (HCAL). The ultimate performance is reached for perfect separation of charged particle clusters from neutral particle clusters in the calorimeter. So, a highly granular calorimeter outside the tracker is needed. A sampling calorimeter with dense absorber material and fine grained readout is proposed. Moreover, ILD detector has the following components:

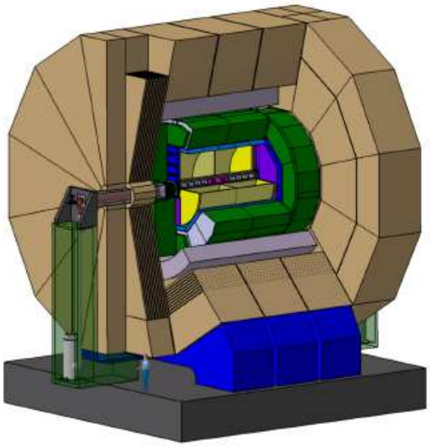

Figure 2.1: *ILD detector concept[13]*

- A system of high precision, radiation hard, calorimetric detectors in the very forward region that extend the calorimetric coverage to almost the full 4π, measure the luminosity, and monitor the quality of the colling beam.
- A large volume superconducting coil surrounds the calorimeters, creating an axial B-field of the 3.5 Tesla.
- An iron yoke, instrumented with scintillator strips or RPCs, to return the magnetic flux of the solenoid, which at the same time, serves as muon filter, muon detector and tail catcher.

The ILD detectors concept is shown in Fig 2.1.

2.2.2 SiD Concept

The Silicon Detector (SiD) concept is based on a silicon tracker, a silicon-tungsten electromagnetic calorimeter, highly segmented hadronic calorimeter, and a powerful silicon pixel vertex detector. SiD also incorporates a high field solenoid, iron flux return, and a muon identification system. Particle Flow Analysis (PFA) is an important consideration for the basic philosophy and layout of the detector. The main features of SiD are([14]:

- the innermost tracking sub-system is the Vertex Detector (VXD), which comprises 5 cylinders and 4 disks on each side of endcap, composed of pixellated sensors closely surrounding the beampipe in 5 Tesla solenoidal field . The cylinder and disk geometry is chosen to minimize scattering and ensure high performance in the forward direction. The VXD sensor technology has not yet been chosen
- for the central tracker SiD has chosen the Si strip technology, arranged as VXDin 5 cylinders and 4 disks on each side endcaps. Particular attention has been dedecated to the endcaps to minimize multiscattering for the forward tracks. The sensors are single sided Si, $\sim$ 15 cm long, with a pitch of 50 μm.The simulations of the integrated tracking system demonstrated high efficiency track finding and excellent momentum resolution [14];
- SiD calorimetry is optimized for jet energy measurement, and it is based on a Particle Flow Analysis as described for ILD. The separation of the energy deposited by charged particles in the calorimeters from energy deposited by photons and neutral hadrons requires highly segmented readout, both transversely and longitudinally. SiD calorimetry begins with a dense, highly pixellated Silicon-Tungsten electromagnetic section (ECAL). The ECAL is made of alternating layers of W and silicon pixel detectors arranged in 1024 hexagonal pixels and forming an imaging calorimeter with a track resolution of $\sim$ 1 mm. The same

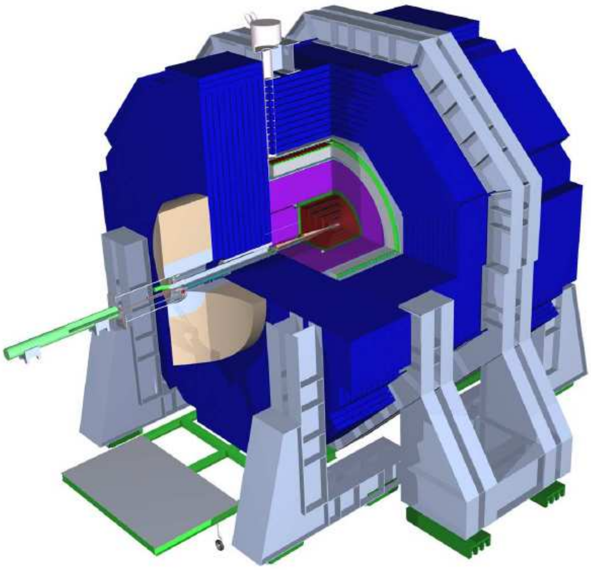

Figure 2.2: *SiD detector concept [14]*

technology is used in the endcaps.

The Hadronic Calorimeter (HCAL), following ECAL, is made of 4.5 λ of layers of steel and detectors. The baseline detectors are RPCs with 1 cm square pixels inserted into the 8 mm gaps between the steel layers. The same technology is used in the endcaps.

The calorimetric coverage is completed, in the forward direction, by a LumiCal and a BeamCal. The LumiCal overlaps the endcaps ECAL and is made of Si-W with the pixellation designed to optimize the luminosity measurement precision. The BeamCal is placed at the smallest forward angle and mounted to the iner side of QD0. Both calorimeters are designed for a 14 mrad crossing angle. SiD detector is shown in Fig 2.2.

- The SiD 5 Tesla superconducting solenoid is based on the CMS design

[16], but has six layers of conductor. The critical cold mass parameter, namely the stored energy/Kg is similar to CMS one.

The flux is returned with an iron structure, configured as a barrel with movable endcaps. The flux return acks as absorber for the muon identifier and is an important component of SiD self shielding.

2.3 The 4^{th} Concept

The 4^{th} Concept is the most innovative proposal for a detector at the ILC. This concept differs from the other two concepts in several respects. In contrast to the particle flow calorimetry adopted in the other two concepts, the 4^{th} Concept utilizes a novel implementation of compensating calorimetry, which balances the response to hadronic and electromagnetic shower components and so it is insensitive to fluctuations in the fraction of the electromagnetic energy in hadronic showers. The 4^{th} Concept is innovative in other respects as well, incorporating dual solenoids and endcaps coils to manage the magnetic flux return and allow for precise muon spectrometer. The detector consists of four basic subsystem:

- a pixel vertex detector (VXD) for high precision measurements of the impact parameter, flavor tagging and near-beam occupancy resolution;
- a low mass, cluster-counting drift chamber (CluCou, KLOE-style) which has timing and pattern recognition capabilities midway between a higher ranularity silicon tracker and a slower, 3-D space point information provided by a TPC, and it is superior to both because of its low multiple scattering contribution to momentum measurement.
- a high precision dual-readout fiber calorimeter (HCAL), complemented

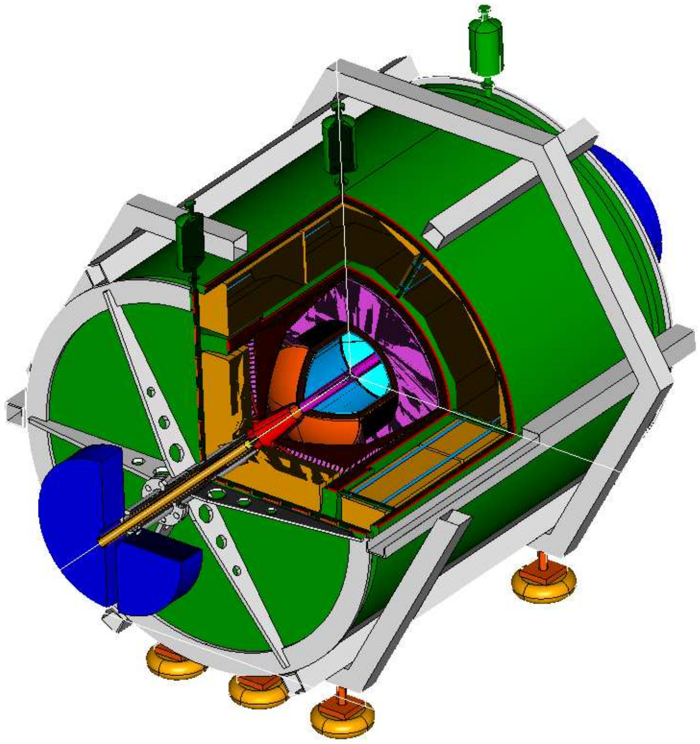

Figure 2.3: 4^{th} *Concept detector [15]*

with an electromagnetic dual-readout crystal calorimeter (ECAL), for the energy measurement of hadrons, jets, electrons, photons, missing momentum and the tagging of muons;

- an iron free dual-solenoid muon system with drift tubes for the inverse direction bending of muons in air to achieve good acceptance and a high muon momentum resolution.

Vertex Detector

The pixel vertex detector follows the same design as the one of SiD, scaled in size to take into account the reduced magnetic field of the 4^{th} Concept. It is a

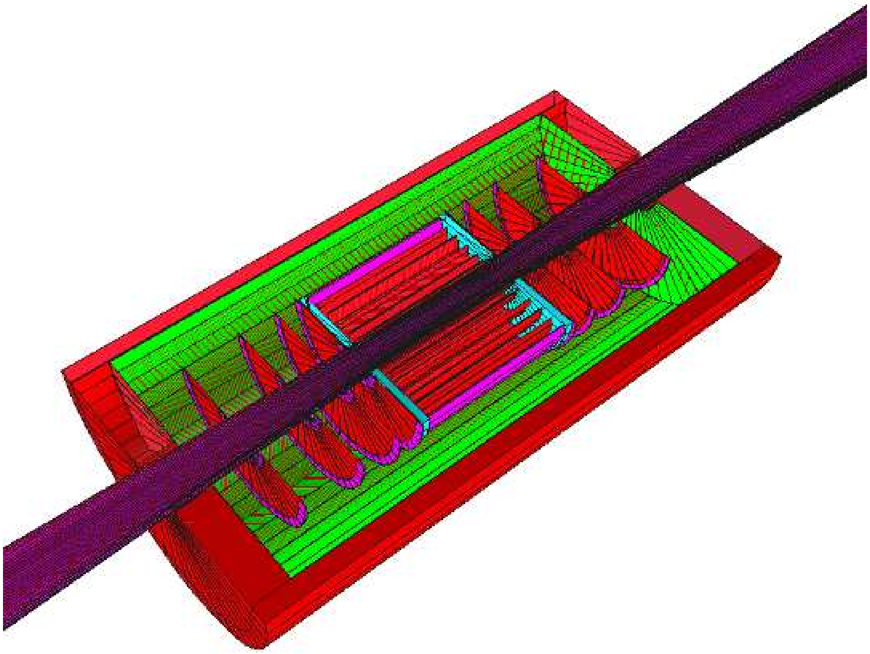

Figure 2.4: 4^{th} *Concept detector: Vertex Detector (VXD simulated in ILCroot Sect.2.4)*

multi Giga-pixel chamber with cylinders and disks. The barrel is made of five layers of staggered silicon detectors covering angular range $134° > |\theta| > 46°$. The basic building block of the barrel part is a ladder consisting of a 100 μm thickness silicon sensor and a readout chip on top of it. Each ladder is mounted parallel to the z direction long stave. The staves are mounted on a carbon-fiber support and cooling sector. Each sector supports five staves. Twelve sectors are mounted together around the beam pipe to close full barrel. A thermal shield made of 100 μm thick carbon fiber encloses the vertex barrel at $r = 12$ cm(Fig. 2.4)

The endcaps have four disks of silicon detectors on each side providing good hermeticity for $|\cos\theta| < 0.994$.

The basic building block of the endcaps of VXD is a trapezoid. Each trapezoid consist of silicon sensor with a thickness of 100 μm and a readout chip on top of it. Twelve trapezoids contribute to make each disk of the endcaps. The VXD provides spatial coordinates on charged tracks for momentum measurement when combined with central tracker and measures the impact parameters of all charged tracks for tagging of heavy quarks (b, c) and the τ lepton. It is expected that this detector will achieved an impact parameter resolution of

$$\sigma \approx 5\mu m \oplus 10\mu m/p \sin^{3/2}\theta \oplus 10\mu m/\sqrt{p}$$

with pixel of $\sim 20\mu$m $\oplus$ 20μm. The layout of the VXD is shown in Fig.2.4.

Drift Chamber

The main tracking chamber proposed by the 4^{th} Concept is a cluster timing drift chamber (CluCou), with full stereo wires for a precise reconstruction of tracks in space. CluCou is modeled on the successful KLOE main tracking chamber that is one of the largest, highest performance and most transparent tracking chambers ever built [17] which has operated successfully for over 10 years. The CluCou allows for a very low multiple scattering contribution to momentum measurement due to a Helium based gas mixture and a light carbon fiber structure. The chamber volume is a cylinder, with spherical end plates, of 19.0 cm inner radius, 150 cm outer radius with 300 cm length at the outer radius and 420 cm at the inner radius. The inner cylindrical wall is made of a thin carbon foil coated by a 20μm aluminium layer for electrostatic continuity. The outer wall is made of twelve carbon fiber aluminium hexcell sandwich panels held by 12 structural struts made of unidimensional carbon fiber. The chamber layout is made of concentric *ring* of wire, grouped to form *superlayers*. Alternating superlayers have stereo angles of opposite sign to

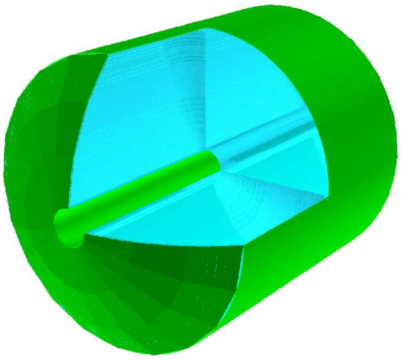

Figure 2.5: *The* 4^{th} *Concept Detector: Drift Chamber (DCH simulated in ILCroot)*

project the particle trajectories onto two independent planes, for efficient three dimensional track reconstruction. CluCou is shown in Fig. 2.5.
The stereo drop δ has chosen constant for all rings, $\delta = 4$ cm, corrisponding to stereo angle inthe range from 55 mrad at the inner radius to 213 mrad at the outer one, so the cell deformation along its length is minimized. The sense wires are 20 μm diameter gold plated tungsten and the field wires are 80 μm diameter silver plated aluminium. The total contribution to the momentum measurement due to the multiple scattering the wires and in the gas is of $3.7 \times 10^{-3} X_0$. The He gas mixture also has a low drift velocity allowing for the cluster timing technique [27] to clocks in individual ionization clusters on sense wires providing an estimated 50 μm spatial resolution per point, a $\frac{dE}{dx}$ resolution near 3% and z-coordinate information on each track segment through an effective dip angle measurement. The drift time in each cell is less than the beam crossing interval and therefore this chamber integrates only one event per readout with no pile ups More details of the drift chamber can be found in Chap 3 Sec 3.4

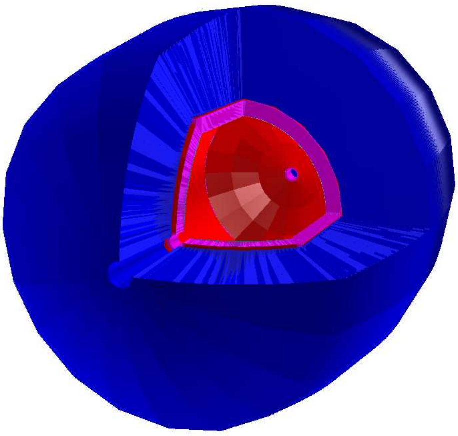

Figure 2.6: *The 4^{th} Concept Detector: Electromagnetic and Hadron Calorimeter (ECAL (red) and HCAL (blue) simulated in ILCroot)*

The Hadronic and ElectroMagnetic Calorimeter

The 4^{th} Concept calorimetry strategy differs from what is adopted in the SiD and ILD Concept. In contrast to the particle flow, the 4th concept utilizes a novel implementation of compensating calorimetry which balances the response to hadrons and electrons,therefore, is insensitive to fluctuations in the fraction of electromagnetic shower. The hadron calorimeter (HCAL) consist of projective towers of dual readout fiber sampling calorimeters to measure separately the hadronic and electromagnetic component of shower and to provide compensation and excellent hadronic energy resolution. The HCAL calorimeter has an expected electromagnetic resolution of $\sigma_E/E = 20\%/\sqrt{E}$, limited by photoelectron statistics [15]. Therefore, an EMCalorimeter is also considered which is based on a crystal calorimeter, with readout of both Cerenkov and scintillation light to provide compensation and which is placed

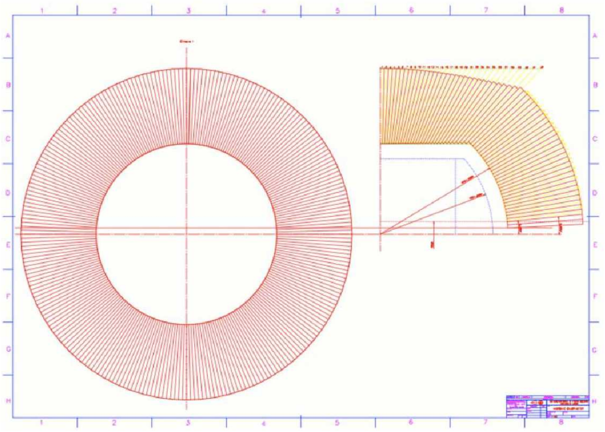

Figure 2.7: *Azimuthal segmentation of the hadronic calorimeter at z=0. At left the r-z projection where one can see the segmentation of concentric tower of the endcaps. In blue are the contours of DCH and the space between the chamber and the fiber calorimeter is filled withe the crystal EM calorimeter [15]*

directly before the fiber towers. The 4^{th} Concept calorimeter is shown in Fig 2.6. The HCAL is a copper matrix loaded with 1-mm diameter alternating scintillating and Cerenkov light fibers every 2 mm. The angular transverse segmentation into projective towers is $\sim$ 1.4 degrees, corrisponding to an innere area of about $4 \times 4cm^2$ $(4 \times 6cm^2)$ depending on θ. There is no longitudinal segmentation and the HCAL depth is 1.5 m, corresponding to a total absorption length of 7.3 λ. The two endcaps have an exact spherical shape following the tracking chamber. HCAL covers the whole solid angle down $\theta \approx \pm$ 2.8 degrees around the beam axis. The outer faces of the towers has a size almost twice that of inner side.

The scintillation and the Čerenkov fibers are grouped, at the outher side, in separated bunches and readout by their respective photoconverter detectors [15].

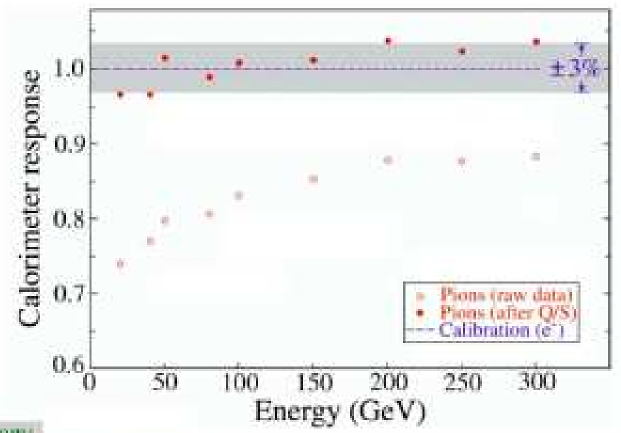

From:
NIM A537 (2005) 537

Figure 2.8: *Linearity of the hadronic response of the fiber DREAM module from 20-300 GeV. Open circles are for single-readout; solid circles are for dual-readout. Data from Ref.[15]*

Fig 2.7 shows the azimuthal projection at $z = 0$ and r - z projection of the hadronic calorimeter.

The ECAL follows the same shape as that of the HCAL. Its basic building block is a $\sim$ 25 cm long BGO projective crystal.

There are 2 x 2 crystal in front of each tower of the fiber calorimeter.

The dual-readout principle is to measure the electromagnetic fraction, f_{em} in each event and directly correct for different responses event-by-event. There are two unknowns in each shower, the shower energy E and f_{em}, and two measurements, the scintillating signal S and the Cerenkov signal Q. The f_{em} is determined by the ratio Q/S and E calculated as combination of Q and S properly weighted by their EM and no-EM part calorimeter response. The hadronic response of this dual readout calorimeter is demonstrated to be linear in hadronic energy from 20 and 300 GeV, despite having been *calibrated only with 40 Gev pions* [15].

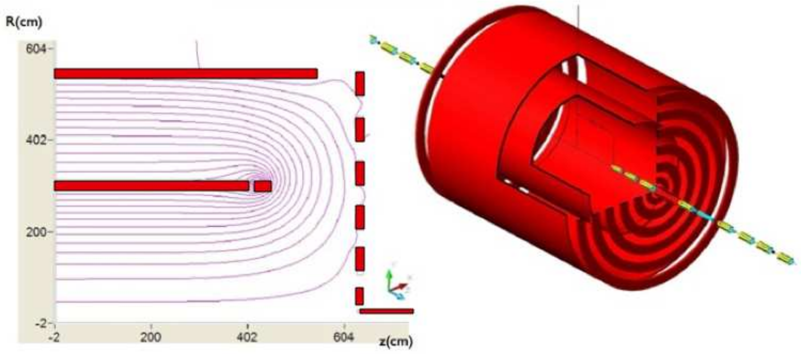

Figure 2.9: *The magnetic field conguration of the dual solenoids.*

This is a critical advantage at the ILC where calibration with 45 GeV electron Z decay could suffice to calibrate the device in a range up to 10 times this energy for physics studies (see Fig 2.8).

Muon-Spectrometer and Magnetic field configuration

The muon system employs a dual-solenoid magnetic field configuration in which the flux from the inner solenoid is returned through the annulus between this inner solenoid and an outer solenoid oppositely driven with a smaller turn density.

The magnetic field in the volume between the two solenoids will back-bend muon which have penetrated the calorimeter and it allows, by means of tracking chambers, independent momentum measurement. This will achieve high precision without the problems of multiple scattering in the flux return in yoke that limits momentum resolution in conventional muon system to 10%. The dual-solenoid field is terminated by a “wall of coils” that provide full contrainment of the field lines and muon bending down to small angles. They also allow for good control of the magnetic environment on and near beem line. The design is shown in Fig 2.9.

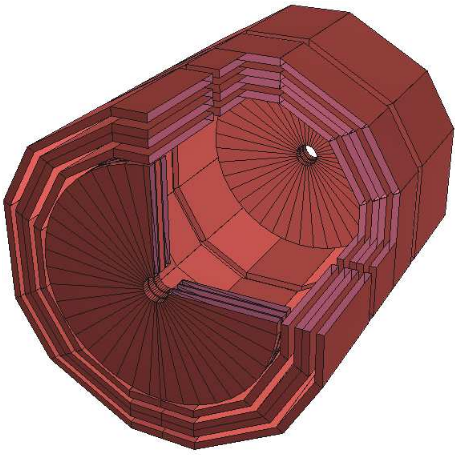

Figure 2.10: *The 4^{th} Concept Detector: Muon Spectrometer (MUD simulated in ILCroot)*

The Muon Spectrometer (MUD) is located in the region between solenoids. The basic element is an high spatial precision drift aluminium tube with cluster counting electronics to reconstruct muons. The barrel consists of three staves each containing 6 trapezoidal sectors. Three chambers are mounted into each sector. Each chamber contains 10 layers of tubes, 4 meters long. So the total length of the barrel is 12 meters, covering the range of ± 45 degrees in θ. The endcaps have a dodecagonal shape, perfectly matching the front shape of the barrel. Each endcap is made of 3 planar sectors rotated by 120 degrees with respect to each other in order to have three independent projections, each of 6 tubes. By studies of the pt resolution of isolated muons in the Muon Spectrometer results that momentum resolution is of σ_{pt} =1.6 x 10^{-3} at high momentum, while for lower momentum tracks it is dominated by the multiple scattering in the aluminium tubes. More details of the Muon Spectrometer can be found in Chap 3 Sec 3.5

2.4 ILCRoot Framework

An optimal choise of the software systems at adopted in the initial phase of a new project is very important because in the majority of the cases, the software apparatus used in the design phase of the project is also adopted in the offline systems of the experiment. We have set a number of guidelines for the implementation of ILCroot [18], the software and offline framework of the 4th Concept:

- Use of public domain common tools. This way we can rely on the huge amount of tools the HEP community has developed in the past.
- Impose a single framework. The simulations, reconstruction, Offline systems and analysis will all be made within the same framework.
- Adopt ROOT as software infrastructure [19]. ROOT is probabEP community. All needed functionalities are present (from data taking to final plots). Reconstruction and analysis are naturally developing in the same framework. Furthermore, it has extensive support from the largest laboratories as CER, FNAL and KEK. It has an unprecedented large contributing HEP Community. It is an Open Source, mutplatforms project, supporting multi-threading and asynchronous I/O. Optimised for different access granularity (Raw data, DST's, NTuple analysis)

We also impose a number of requirements on the software framework, to be built over the ROOT infrastructure. Such requirements are needed to garantee the easy of use by several groups, possibly located in distant places and also to garantee that the system can evolve smoothly into a full Offline systems to be used when the experiment is running. The main requirements on the software framework are the following:

- Scalability. This is essential to guarantee that, increasing the number of processing nodes, we also increasi the troughput from the offline systems.
- Portability. When this feature is satisfied, the same code is able to run on different computing systems.
- Multiplataform. This requirement is essential when computing farms are built using different computers or operating systems.
- High level of modularity. This is a guarantees for easy of maintenance and development. We want to pursue modularity of the framework by imposing the absence of code dependencies between different detector modules and by designing the structure of every detector package in a way that static parameters (i.e. geometry and detector response parameters) are stored in distinct objects.
- The data structure has to be built up as ROOT TTree-objects. The access to the data will occure efficiently either to the full set of correlated data (i.e., the event) or to only one or more sub-sample (one or more sub-detectors).

ILCroot derives from AliRoot, Alice's Offline framework[20]. The entire architecture and the structure of the classes have been inherited by the original with few, minor changes, needed for the simulations of an experiment to an electron-positron collider. The detector modules, containing the decription and the functionnalities of the 4th Concept sub-detectors. The modularity of such framework easily allows replacing existing detector modules with new ones specific to the detector that is being simulated.

The architecture of ILCroot is briefly descibed here.

A STEER module provides steering, run management, interface classes, and base classes to the entire framework. The detectors are independent modules that contain the code for simulation and reconstruction while the analysis code is progressively added. Detector response simulation is performed via the Virtual Montecarlo (VMC) technology[21]. The user code is all in C++, including the geometry definition. All the user−defined parameters (including the event generator and the kinematics of the event) are included in a plain C macro−file ("$Config.C$") which is interpreted at execution time by the ROOT interpreter ($CINT$). simulation and reconstruction are special services also controlled by the Run Manager class. The base class for each subdetector module is the Detector Class . Both sensitive modules (detectors) and non-sensitive ones are described by this base class. The Detector class supports the hit and digit trees produced by the simulation and the the objects produced by the reconstruction. This class is also responsible for building the geometry of the detectors. The Virtual MC provides a virtual interface to the Monte Carlo. It enables the user to build a Monte Carlo application independent of any actual underlying Monte Carlo implementation. Detector response simulation can be performed via different transport codes like GEANT3[22], GEANT4[23], and FLUKA[24]. The concrete Monte Carlo is selected and loaded at run time. The VMC is a separate package running on top of ROOT along with the real Montecarlo's packages and any other external package. It interacts with ILCroot main reconstruction program through the Run Manager which sends calls to the VMC whenever needed.

The interface with the event generator is implemented through a special class called TGenerator. TGenerator is an abstract base class that defines the interface of ROOT and the various event generators. It allows easy mixing of signal and background and, furthermore, it provides the user with an easy and coherent way to study a variety of Physics signals.

The Simulation Process

The simulation and reconstruction processes occur through the following passes:

- **Event generation.** The collision is simulated by a physics generator code or a parametrization and the final-state particles are fed to the transport program.
- **Particle tracking**. The particles emerging from the interaction of the beam particles are transported in the material of the detector, simulating their interaction with it, and the energy deposition that generates the detector response (hits).
- **Signal generation and detector response.** During this phase the detector response is generated from the energy deposition of the particles traversing it.
- **Digitization.** The detector response is digitized and formatted according to the output of the front-end electronics and the data acquisition system. The digitization process is split into two parts: the production of summable digits (*SDigitization*) and the final *Digitization.* In the first step, the response of the electronics to the passage of one individual particle is simulated in the assumption that no pile-up occurs. In

the second step, the *SDigits* from several tracks corresponding to the same read−out channel are summed togheter.

- **Clusterization.** This pass is also called *pattern recognition.* In this phase the *Digits* are searched trough and separated in list associated with potential reconstructible particles. If the shape of one *Cluster* is such that it contains the contribution of two particles, an unfolding algorithm is called were we attempt to recover the signal belonging to each subcluster.

- **Reconstruction.** In this pass, the *Clusters* found are analized and the kinematic informations of the track are evaluated. The reconstruction of the particles in the subdetectors proceeds trough two phases: *Local* and *Global Reconstruction.* The *Local Reconstruction* is perormed by the specific detector module and it handle both the reconstruction algorithms and the corresponding data. ILCroot modularity imposes that the local reconstruction in one detector module is totally unrelated to any other module, with no exchange of data of any sort. Therefore, several version of the of a certain detector can coexist with no interference. The *Global Reconstruction* integrates toghether the data posted by the several detector modules partecipating (for example, the three tracking detectors: Vertex Detector, Drift Chamber and the Muon Spectrometer) and perform the final reconstruction.

    - **Local Reconstruction** Each particle going through the detectors leaves a number of hits at the position in space where it has traversed the sensitive material. These simulated space−points signals needs to be associated to the same particle we are trying to reconstruct. The *clusterization* is very detector specific; therefore it is handled by a dedicated class per each detector module simulated.

- **Global Reconstruction** The reconstruction algorithm of the charged tracks is performed by a Parallel Kalman Filter algorithm[25]. The implementation of such method has been imported by the Alice experiment (Aliroot [20]) which has a very good success in reconstructing tracks in their large multiplicity environment.[26]. The reconstruction algorithm is able to cope with non-Gaussian noise and ambiguous measurements. To gain almost optimal results, so called Maximum Information Approach (MIA) is applied. An incremental approach to combined reconstruction was chosen. Algorithms and data structures are optimized for fast access and usage of all relevant information. The event reconstruction starts with the determination of the position of the primary vertex. This can be done prior to track finding by a simple correlation of the space points reconstructed at the first two layers of the Vertex Detector. The information about the primary vertex position and its position uncertainty is then used during the track finding (seeding and applying the vertex constraint) and for the secondary vertex reconstruction. The combined track finding−fitting in the 4th Concept detectors consists of three passes:

    1. Initial inward reconstruction pass. The overall track finding starts with the track seeding in the outermost layers of the drift chamber. Then, for each track reconstructed in the drift chamber, its prolongation in the Vertex Detector is obtained.
    2. Outward reconstruction pass and matching with the outer detectors. From the innermost Vertex Detector layer the

   Kalman Filter proceeds in the outward direction. During this second propagation the space points with large χ^2 contributions are removed from the track. Finally, the Kalman filter continues into the Muon Spectrometer where the clusters found are matched to the prolonged track.

   3. Final reconstruction pass. In this pass the primary track is refitted back to the primary vertex or, in the case of the secondary tracks, as close to the vertex as possible. During this pass the secondary vertices are reconstructed (V0s, cascade decays and kinks) and the information is stored in the Event Summary Data (ESD).
   4. VXD Standalone Tracking. The clusters of the VXD which have not been used in the previous steps are fed to the Standalone VXD tracker.
   5. Muon Spectrometer Standalone Tracking. The clusters of the Muon Spectrometer which have not been used in the previous steps are fed to the Standalone Muon Spectrometer tracker.

- **Particle Identification.** The PID informations obtained from each individual detector are combined in a Bayesian way. This approach has the advantage that PID signals of a different nature (e.g. dE/dx and shower shapes) can be combined together even in case of signals distributed according to very different probability density functions.

- **ESD** Raw data, collected by the set of individual sub-detectors of the 4th Concept, are calibrated and objectified into Digits which will contain, at least in principle, the same information carried by the real raw data.

The output of the reconstruction is the Event Summary Data (ESD) containing the reconstructed charged particle tracks (together with the particle identification information), decays with the V0 (like $K_{short} \rightarrow p\pi$ and $\lambda \rightarrow \pi^{+}\pi^{-}$), kink (like charged $K \rightarrow \mu\nu$) and cascade topologies and some neutral particles reconstructed in the calorimeters.

Chapter 3

The 4^{th} Detector tracking subsystems

3.1 Electron transport in gas

When a charged particle traverses a medium, it ionizes atoms and molecules of the medium creating primary ion-pair. The created electrons, if within a field, may acquire sufficient energies to further ionize the medium and to create secondary electron-ion pair. The number of primary electron pair per cm N_p and the number of total electron-ion pairs per cm N_t are characteristic of a given gas or gas mixture and they are important for determining for the spatial resolution of a tracking detector.

The relevant transport parameters for operation of high accuracy drift chambers are drift velocity, longitudinal and transverse diffusion and the characteristic energy of electrons. The 4^{th} Concept has chosen a helium based gas mixtures for its tracking subsystems for the following reasons:

- the large radiation length of helium and thus the lower multiple scattering contribution to the momentum measurement (X_0 as5299 m compared to the argon, X_0=110m).

- a relatively low drift velocity also at high fields, which thus facilitates the time spread of consecutive ionization clusters providing a better position resolution and two track separation thanks to cluster timinig. Drift velocity in $He - iC_4H_{10}$ are of the order of 2 cm/μs at fields around higher than 1 kV/cm.
- the photon absorption cross section in helium is low implying low sensitivity to backgrounds x-rays from synchrotron radiation
- another advantage is the small Lorentz angle in crossed E and B field. The Lorentz angle is the angle of deflection of the electron swarm with respect to the electric field in the presence of a orthogonal magnetic field and it is a function of both fields and it is characteristic of the gas. For argon based mixture, the Lorentz angle is large at small values of electric field and almost independent of the electric and magnetic field values, but above few hundred V/cm, it starts to be dependent on both. This is an especially important source of distortions in detectors having not-uniform geometries. For helium based gases mixture the corresponding Lorentz angles are much smaller than argon based mixture.

Charged particles passing through a medium loose kinetic energy by excitation of bound electrons and by ionization. The latter process is of greater importance as the atomic electrons are detacted from the atom and can be subsequently detected.

Given the momentum of the incident particle $p = \gamma m_0 \beta c$, where γ is the Lorentz factor, $\beta c = v$ and m_0 is the rest mass of the particle, the maximum energy that can be transferred to an atomic electron in a medium is given [28]

$$E_{kin}^{max} = \frac{2m_e c^2\beta^2\gamma^2}{1 + 2\gamma\dfrac{m_e}{m_0} + (\dfrac{m_e}{m_0})^2} = \frac{2m_2 p^2}{m_0^2 + m_e^2 + \dfrac{2m_e E}{c^2}} \tag{3.1}$$

where the kinetic energy E_{kin} is related to the total according to $E_{kin} = E - m_0c^2$. If one neglects the quadratic term in Eq.3.1, which is a good approximation for all incident particles other than electronics, it follows that

$$E_{kin}^{max} = \frac{p^2}{\gamma m_0 + \dfrac{m_0^2}{2m_2}} \tag{3.2}$$

For relativistic particles $E_{kin} \approx E \approx pc$ and the maximum transferable energy become:

$$E^{max} = \frac{E^2}{E + \dfrac{m_0^2c^2}{2m_e}} \tag{3.3}$$

If the incident particle is an electron, these approximations are no longer valid and Eq.3.1 reduces to:

$$E_{kin}^{max} = \frac{p^2}{m_2 + \dfrac{E}{c^2}} = \frac{E^2 - m_e^2c^4}{E + m_ec^2} \tag{3.4}$$

The average energy loss dE per length dx for heavy particles is given by the Bethe-Bloch formula[28]

$$-\frac{dE}{dx} = kz^2\frac{Z}{A}\frac{1}{\beta^2}\left[\frac{1}{2}\ln\frac{2m_ec^2\beta^2\gamma^2E^{max}}{I^2} - \beta^2 - \frac{\delta}{2} - \frac{C}{Z}\right] \tag{3.5}$$

where A, Z, and I are respectively the atomic weight, the atomic number, and the mean excitation potential of the material; z is the particle charge, expressed in unit of the elementary charge e, and βc is its velocity; the constant $k \simeq 0.307$ MeV $g^{-1}cm^2$, δ and C are factors needed to correct respectively the densty and shell effects, E^{max} represents the maximum kinetic energy

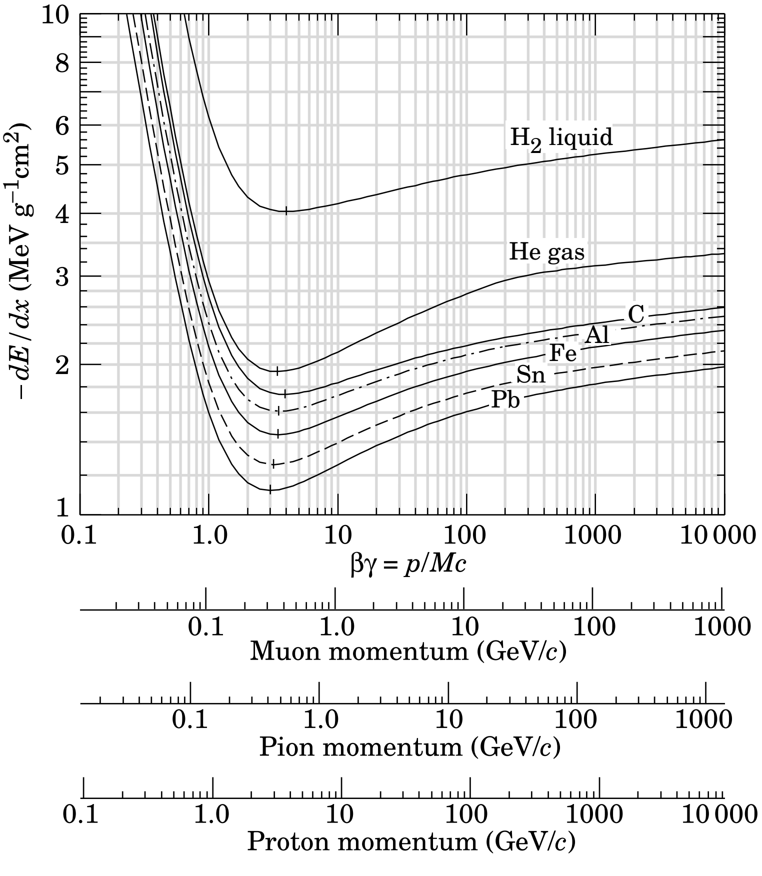

Figure 3.1: *Mean energy loss rate in liquid hydrogen, gaseuos helium, carbon, aluminum, iron, tin, and lead for different particles [28]*

given by Eq.3.1.

Figure 3.1 shows the energy loss rate for several species of incident particles, as a function of the incident particles momentum, passing through several media.

Equation 3.5 gives only the average energy loss of charged particles. For thin absorbers, mainly gases, strong fluctuations around the average energy loss exist. The energy loss distribution for the absorbers is strongly asymmetric and can be parametrized by a Landau distribution that can be reasonable approximated by:

$$L(y) = \frac{1}{\sqrt{2\pi}} \times exp[-\frac{1}{2}(\lambda + e^{-lambda})] \tag{3.6}$$

where λ is deviation from the most probable energy loss.

The Landau fluctuation of the energy loss are related to large extent to very high energy transfers to the atomics electrons, which allow escape and are called δ or knock-on electrons. The large fluctuations of the energy loss are quite frequently not observed by a detector, as detectors only measure the energy which is deposited in their sensitive volume, and this energy may not be the same as the energy lost by particle. Some of the δ electrons may leave the sensitive volume before depositing all of their energy. Eq.3.5 describes the energy loss of the heavy particles. In case of electrons as incident particles, it needs to be consider that, at low energy, the energy loss is influenced by breemsstrahlung.

The energy loss rate depends on the incident particle's electric charge and velocity, but not on its mass. Therefore, if one is able to simultaneously measure the curvature of the track, and, therefore, its momentum, and the deposited ionization energy associated with the track, i.e. its velocity, the incident mass can be identified.

3.2 CLUster COUnting technique

The large and inherent uncertainties in total energy deposition, described by Landau-like distribution functions, represent a serious limitations to the particle identification capabilities. The large variety of secondary processes contributing to the total energy deposition impairs the good statistical properties of the underlying process: the primary ionization, which is clearly poissonian in nature. A method capable of retrieving this fundamental feature from the produced analog signals could recover the good properties of the primary ionization statistics and allow for a more powerful particle identification.

The cluster counting method [30] consists in singling out, in every recorded detector signal, the isolated structures related to the arrival on the anode wire of the electrons belonging to a single ionization act. In order to achieve this goal, special experimental conditions must be met: pulses from electrons belonging to different clusters must have a little chance of overlapping in time and the time distance between pulses generated by electrons coming from the same cluster must be small enough to prevent overcounting. The optimal counting condition can be reached only as a result of the equilibrium between the fluctuations of the processes which prevent a full cluster detection efficiency and of those which enhance the time separation among different ionization events.

A favourable ratio between the mean free path of the ionization particle and the one of the more energetic primary electrons is a requirement that cannot be disregarded. Therefore small specific ionization is needed in order to have a good localization of each cluster along the track and low diffusion to guarantee a limited swelling up of the cluster along the drift path. Gas mixture based on helium [30] are well suited for cluster counting measurements.

3.2.1 Impact parameter measurement

In a 2 cm-radius cylindrical drift tube filled with a helium based gas mixture (90%He 10%C_4H_{10}), the time separation between ionization clusters, for any impact parameter, ranges from a few nanoseconds to a few tens of nanoseconds, depending on the drift distance to the sense wire. On these bases, provided the front-end electronics is such that the rise time of electron signals is below 1 ns and they are digitized at sampling rates of a least 1 GSa/s, single electron counting can be efficiently performed [30].

Multiple electron clusters, about 23% of the total in helium based gas mixture, are identified according to the relative mutual time delays between electrons, since, for short distances the time spread due to electron diffusion within the same clusters is smaller than the time separation between consecutive clusters, and at larger drift distances, corresponding to more than a few mm, while diffusion grows slowly with the square root of distance, the time separation between clusters increases more rapidly because of the linear slowing down of the drift velocity with the electric field.

The expected density of primary ionization clusters in this gas mixture for a m.i.p. is 12.5/cm, with a total number of electrons of about 20/cm. The time, t_1, of the first drifting electron after t_0, the trigger time, gives a good approximation of the impact parameter b relative to the sense wire

$$b = \int_{t_0}^{t_1} v_{drift}(x(t))dt \tag{3.7}$$

The expected number of primary clusters is, therefore:

$$n_{cl} = \frac{2\sqrt{r^2 - b^2}}{\lambda(\beta\gamma)} \cdot \sin\theta \tag{3.8}$$

where λ is the mean path between two ionization acts, which depends on $\beta\gamma$ of the crossing particle, and θ is the dip angle between the track and the sense wire. The expected total number of ionization electrons is n_{ele}, on average 1.6 times the number of primary clusters in this gas.

In general, from the digitized pulse shape, one can reconstruct the ordered sequences of the electron arrival times and their amplitudes based on the time separation between consecutive clusters and on the electron time spread due to diffusion, for any given impact parameter, one can define a probability function which relates the probability that the i^{th} electron belongs to the j^{th} cluster:

$$P(i,j),\ i=1,n_{ele},\ j=1,n_{cl} \tag{3.9}$$

In general the main contributions to the unacertaining in the determination of the impact parameter 3.7 : a) the ionization statistics, b) the electron longitudinal diffusion and c) the time resolution of the electronics. For small impact parameters and for gas mixture with a low primary ionization, the contribution due to the ionization statics is the dominant one. In effect, the definition of eq.3.7, represents a systematic overestimate of b by the quantity Δb, usually, though improperly, referred to as the ionization statics contribution to the impact parameter resolution:

$$\Delta b = d_1 - b = \sqrt{b^2 - \lambda_1^2} - b\lambda_1 \in (0, \lambda/2) \tag{3.10}$$

In principle, the knowledge of the arrival time sequence of all ionization clusters, helps correcting such an overestimate of b allowing for a determination of its value with a resolution, as small as 50 μm. It is worth noticing that most of the improvement in impact parameter resolution is obtained by using only the timing of the first few clusters, with smaller and smaller contribution from the addition of the successive ones, when the improvement is saturated because of the accumulated fluctuations.

3.2.2 Particle Identification dN/dx vs dE/dx

Because of the large Landau fluctuations in the energy deposited in a gas by a charged particle along its trajectory, a traditional truncated mean algorithm will use only a fraction of the total number of ionization clusters produced, reaching a relative resolution of 6%, 4.5% being its theoretical limit. The Poisson nature of ionization deposition allows the counting of the total number of ionization clusters, N, along the trajectory of a charged particle, with a relative resolution of $1/\sqrt{N}$. For the proposed helium gas mixture, N=12.5/cm, and a track length of 1.3 m, one would obtain a relative resolution of $\sim$ 2.5%.

3.3 The 4_{th} Concept Central Drift Chamber

As mentioned in Chapther 2, the 4^{th} Concept adopted as a central tracker a fully stereo Drift Chamber for precise reconstruction of tracks in space (CluCou). A 90%Helium + 10% Isobutane gas mixture and a light carbon fiber structure are chosen to minimize the multiple scattering contribution to the momentum measurement, particularly for momenta below 30 GeV/c. Moreover, the use of the cluster timing technique guarantees good particle identification, of the order of $\sim$ 3%, better spatial resolution and, therefore, good momentum resolution also for high momenta.

3.3.1 CluCou Mechanical Structure and Layout

The chamber volume is a cylinder, with spherical end-plates, of 19.0 cm inner radius, 150 cm outer radius, with 300 cm length at the outer radius and 420 cm at the inner radius. The inner cylindrical wall is made of a thin, 0.2 mm, carbon fiber foil coated by a 20μm aluminium layer for electrostatic continu-

ity, equivalent to 0.001 X_0 in the terms of material budget. The outer wall, equivalent to 0.018 X_0, is made of twelve carbon fiber aluminium hexcell sandwich panels held by 12 structural struts made of unidimensional fiber.
The dome shaped end walls, with a radius of curvature of 212 cm, are made of 5 mm thick carbon fiber (equivant to 0.029 X_0) to contain the gas volume and to hold in place all the wires at the right tension (equivalent to $\sim$ 15 T). Construction details are given in ref. [15].
The chamber layout is made of 24 concentric *superlayers*, each consisting of 12 *rings*, the first and the last being shared with the preceeding and the following superlayer. The superlayers are string at stereo angles of alternating opposite signs so that the particle trajectories are projected onto two independent planes, for efficient three dimensional track reconstruction. The basic element of CluCou is a hexagonal shaped cell with size varying from 0.4 cm, at innermost radii, to 0.7 cm. For the gas mixture proposed and at the necessary gain, the maximum drift time is contained within one buch crossing (less than 350μm.
In the $x-y$ plane at z = 0, for every ring of each superlayer, the total number of wires $n_w = n_{sw}+n_{fw}$ is costant, where n_{sw} is the number of sense wires (20 μm diameter gold plated tungsten) and n_{fw} is the number of field wires (80 μm diameter silver plated aluminium) with n_{fw}=2n_{sw}. The distance between two consecutive wires positioned in the r^{th} ring within the s^{th} superlayer is given by

$$d_{rs} = r_{rs} \cdot \phi_s, \quad \phi_s = 2\pi/n_r^w \tag{3.11}$$

where r_{rs} is the radius of the r^{th} ring within the s^{th} superlayer and n_r^w the total number of wires in the ring. The sequence of wire is rotated by 3/2 d_{rs} from rth ring to the next (r+1)th. The pitch between two consecutive rings,

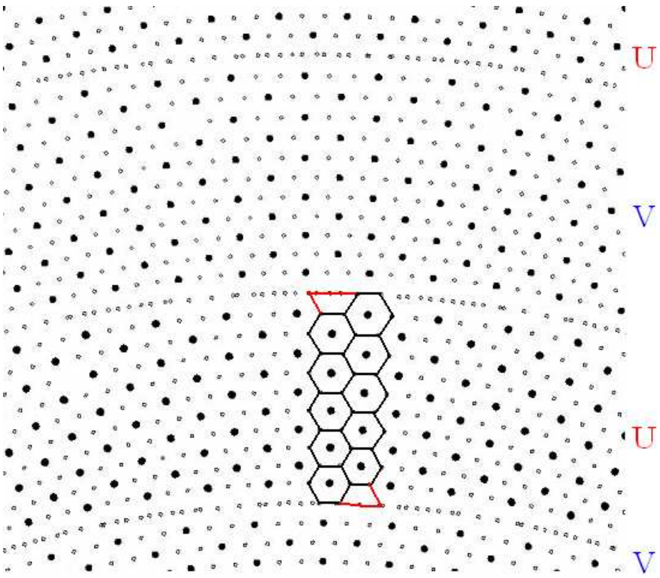

Figure 3.2: *Hexagonal cells per s^{th} CluCou superlayers*

Δr_{rs}, is $\Delta r_{rs} = d_{rs} \sin 60$ so that, for every three consecutive rings ($r_{r-1,s}$, r_{rs}, $r_{r+1,s}$), it is possible to build n_{sw} perfect hexagonal cells, whose vertices are given by 6 field wires with the sense wire positioned at the center, Fig. 3.2. For CluCou we have chosen the configuration with $n_1^{sw} = 100$ cells per rings at the first superlayer, and to $n_{24}^{sw} = 460$ at the last. In order to keep the cell size as costant as possible throughout the 24 superlayers, the generic superlayer s must have the following number of cells in each ring:

$$n_s^{sw} = 100 + \ (s-1)\Delta n_{sw} \quad s \in (1, 10) \tag{3.12}$$

with

$$n_s^{sw} = 100 + \ (s-1)\Delta n_{sw} \quad s \in (11, 19)$$

$$n_s^{sw} = 100 + \ (s-1)\Delta n_{sw} \quad s \in (11, 19)$$

where $\Delta n_{sw} = 20$.

The total number of sense wires is 66020, while the total number of field wires is 152080.

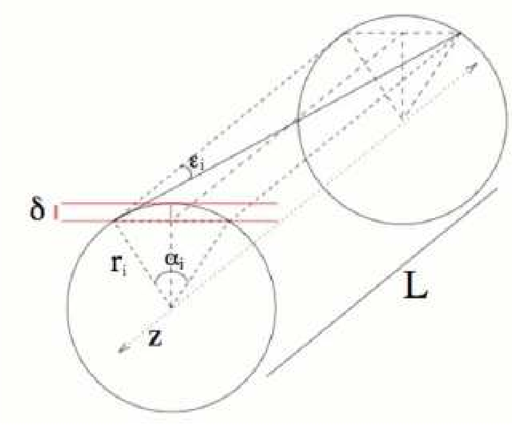

Figure 3.3: *Sketch of a stereo wire with the denition of stereo drop* δ *and of stereo angle* ϵ_i

Among all possible arrangements of a stereo configuration of wire, we have chosen the one which minimizes the cell deformation along its length. This is equivalent to set the stereo drop δ constant for all rings 3.3. The stereo angle is

$$\varepsilon_{ring} = tan^{-1}\left(\frac{r_{ring}\sqrt{1-\left(\frac{r_{ring}-\delta}{r_{ring}}\right)^2}}{l}\right)$$

where l is the half length of the wire taking into account the spherical dome shaped end plates of CluCou. A drop of 4 cm we have that the stereo angles values are in the range 55 mrad for the first ring to 213 mrad for the last one (fig.3.3.

With the proposed layout, more than 90% of the chamber volume sampled (crf. fig. 3.2). The total contribution to the momentum measurement due to the multiple scattering in the wires and in the gas is 1.1×10^{-3} X_0 and 1.6×10^{-3} X_0, respectively for the W sense wires and the Al field wires and 1.0×10^{-3} X_0 for gas mixture, for a total of 3.7×10^{-3} X_0

3.3.2 Front end

Although the cluster timing technique features a number of advantages, the bottleneck for its implementation is represented by the difficulties in realizing a low cost, high-speed, low-power electronic interface being able to process such signals. A CMOS [29] 0.13 μm integrated circuit made of a fast preamplifer (with -3dB bandwidth of 700 MHz) plus a 1 Gsa/s 6-bit ADC has been designed. Details of the design of the chip can be found in ref. [29]

3.3.3 CluCou Performances

Geometry Description

In the geometry class DCH I have implemented the algorithm to describe the CluCou geometry. Such geometry reflects the version of CluCou with spherical end plates, described at Sec 1.4.1. The description of the volumes and materials is quite accurate, including each single wire, both sense and field, to take into account the effect of kinks on tracks hitting the wires and multiple scattering in the materials.

Detector Simulation

The implementation of the detector response to the passage of a charged particle uses an approximate algorithm to simulate the Cluster Counting readout. In the simulation class DCH I have implemented the algorithm to simulate the individual ionization act in gas mixture when traversed by a charged particle. The algorithm is obtained by a preliminary study of the energy loss distribution of a charged particle for a He-based mixture(90% He + 10% C_4H_{10}) simulated with **Garfield** [31] and **Magboltz** [32]. Magboltz, numerically solves the Boltzmann transport equation to compute the elec-

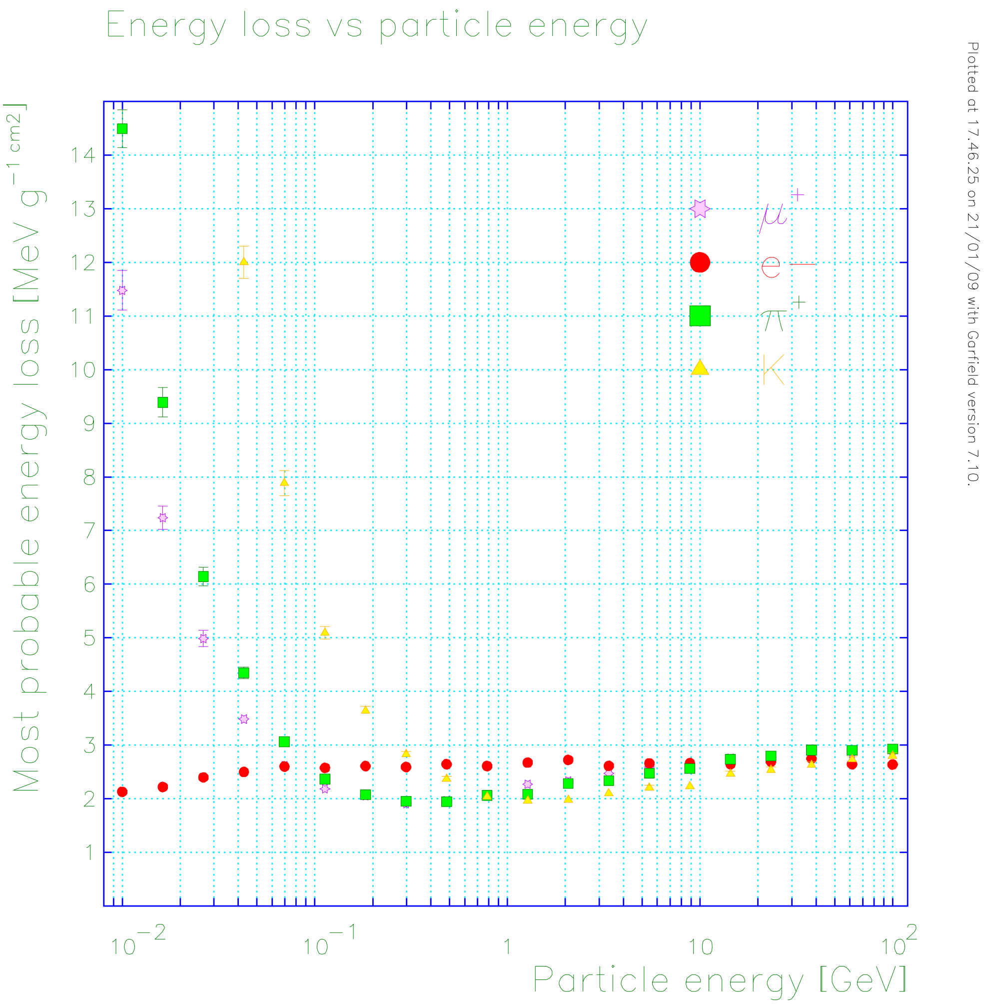

Figure 3.4: *Energy loss distribution of different particles as function of their momenta*

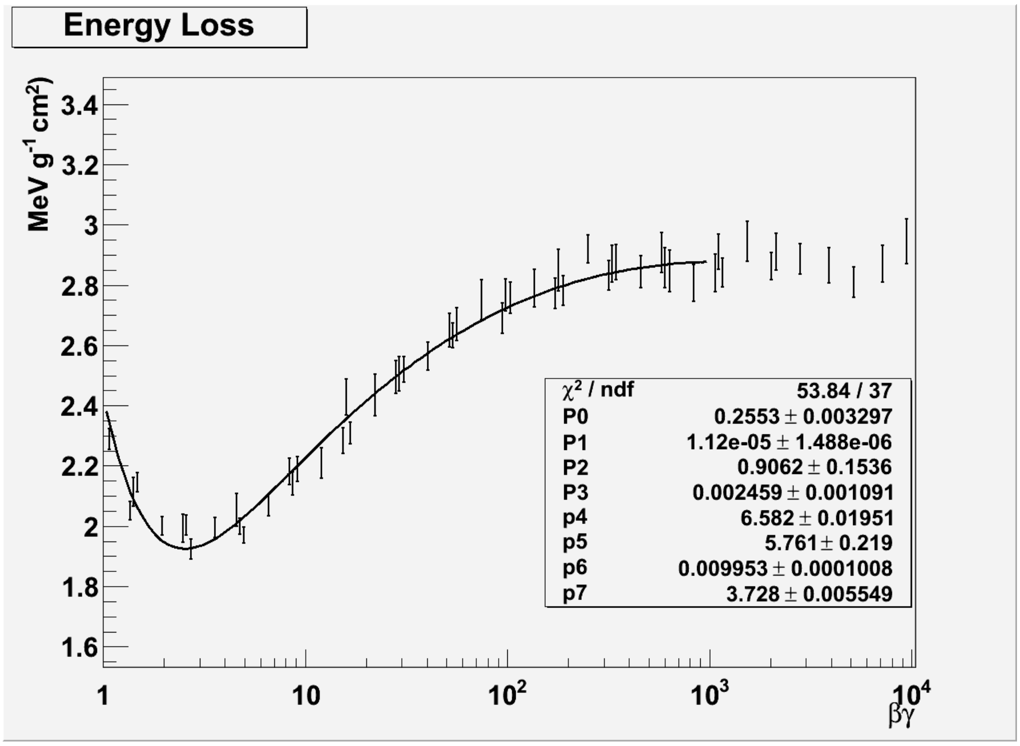

Figure 3.5: *Fit of the energy loss distribution of particles as function of* $\beta\gamma$

tron transport parameters in the gas mixture and Garfield, for a designed gaseous detector computes the electromagnetic field maps, the electron and ion transport lines and the signals produced on the wires.
In Fig 3.4 energy loss distribution of different particles as function of their momenta is shown. In Fig 3.5 is shown the fit of the energy loss distribution of particles as function of $\beta\gamma$.

The algorithm to simulate the Cluster Counting readout, has been chosen in order to speed up the calculations, otherwise overwhelmingly slow given the number of volumes of CluCou. However, all the features of the Cluster Counting technique have been implemented, the most notable being the loss of resolution and efficiency when more than one track is crossing the same cell. In this case, we associate a single hit resolution of $55\mu m$ to the closest to the sense wire track and $120\mu m$ to the second track. Any other track is assumed lost. The correct implementation of such behaviour is very important when events with many tracks are considered or when the beam pair background is taken into account. Fig.3.6 and Fig. 3.7 show, the cell occupancy and track molteplicity per superlayer for the highest molteplicity events $e^+e^- \to t\bar{t} \to 6jets$

Detector Reconstruction

A reconstructable track is defined as a track with a distance of closest approach to the origin less than 3.5 cm and with a least 10 hits in the drift chamber or at last 4 hits in the vertex detector. Such tracks have an almost 100% probability to be successfully reconstructed by the pattern recognition algorithm and by the Kalman Filter fit procedure. The resolutions obtained for the 5 track parameters after the pattern recognition and Kalman Filter are shown in Fig 3.8 as a function of transverse momentum P_T of single

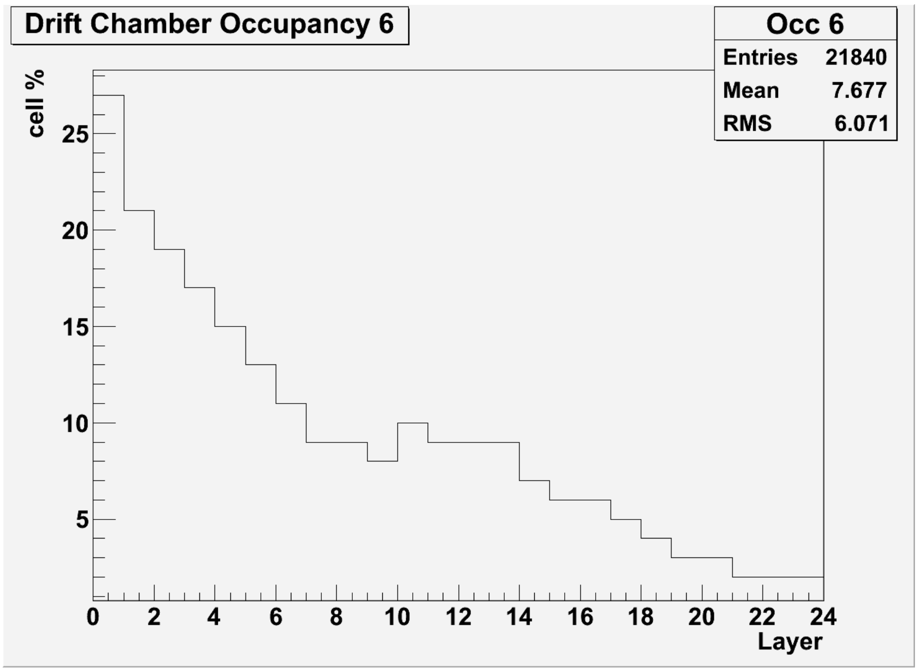

Figure 3.6: *Cell occupancy per superlayer for events* $e^+e^- \rightarrow t\bar{t} \rightarrow 6jets$

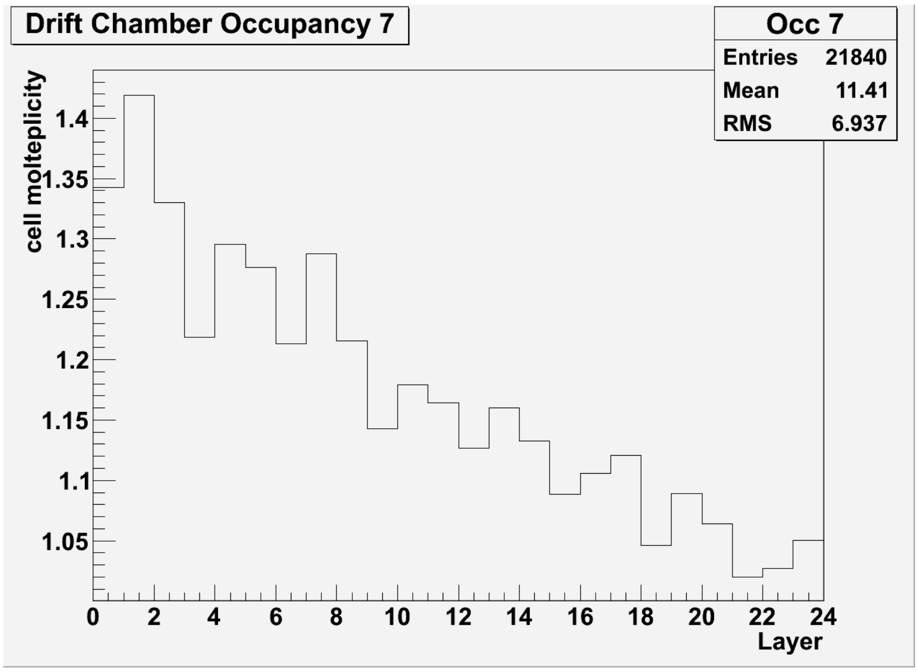

Figure 3.7: *Track molteplicity per superlayer for events* $e^+e^- \rightarrow t\bar{t} \rightarrow 6jets$

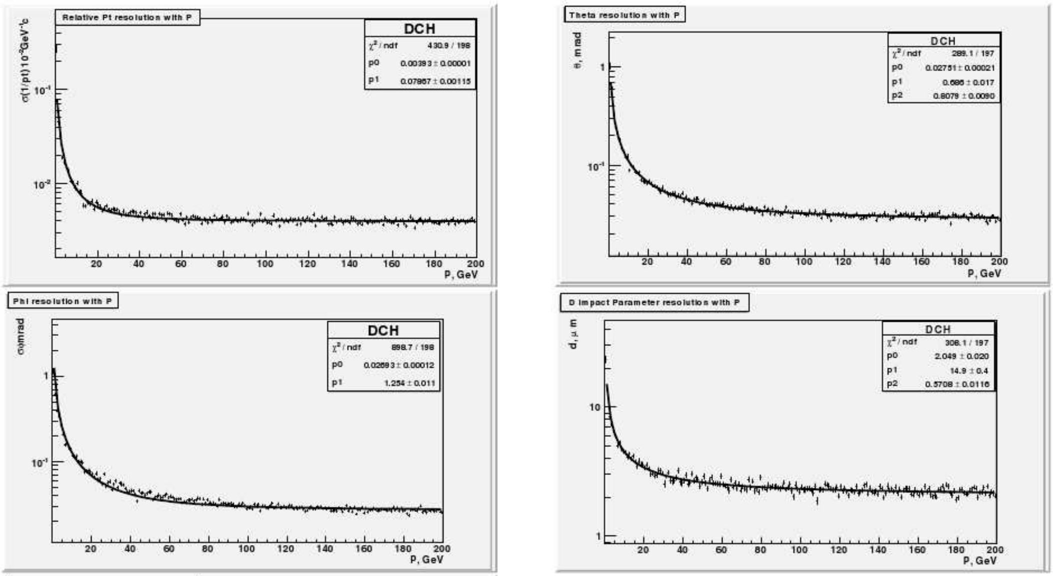

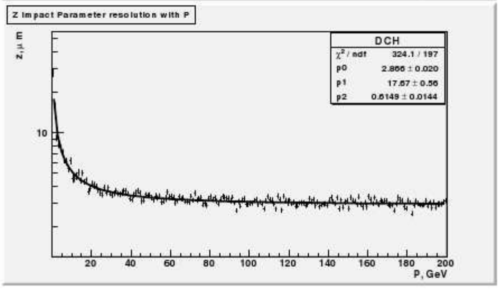

track parameter	fit results stochastic term	multiple scattering term
$\sigma(1/p_T)$	3.9×10^{-5} (GeV/c)$^{-1}$	$\oplus$ $7.9 \times 10^{-3}/p_T$
σ_θ	0.69 mrad/$p_T^{0.80}$	$\oplus$ 0.027 mrad
σ_ϕ	1.25 mrad/p_T	$\oplus$ 0.027 mrad
σ_d	14.9 μm/$p_T^{0.57}$	$\oplus$ 2.0μm
σ_z	17.7 μm/$p_T^{0.58}$	$\oplus$ 2.9μm

Figure 3.8: *CluCou resolutions as a function of transverse momentum P_T of single muons in the range [0,200] GeV.*

Track Parameter	Fit results
$\sigma(P_t^{-1}$	$7.9/P \oplus 0.39 \times 10^{-4}$ GeV
$\sigma(\theta)$	$0.62/P^{0.79} \oplus 0.027 mrad$
$\sigma(\phi)$	$1.3/P \oplus 0.031 mrad$
$\sigma(D_o)$	$12.8/P^{0.48} \oplus 2.1 \mu m$
$\sigma(Z_o)$	$15.7/P^{0.58} \oplus 2.9 \mu m$

Figure 3.9: *Parameters from a fit to the momentum resolution distributions.*

muons in the range [0,200] GeV. The parameters from a fit to the above distributions are summarized in Fig 3.9. The momentum resolution reached can be parametrized as: $\sigma(1/p_T) = 3.9 \times 10^{-5} \oplus 7.9 \times \times 10^{-3}/p_T \ (GeV/c)^{-1})$. These results are comparabile with those obtained in the case of a TPC or of a Silicon tracker. The performance are in line with goal values for tracking detector at the ILC.

3.4 The Muon Spectrometer

The muon system consist essentially of a Spectrometer inserted between two solenoids whose magnetic field configuration is shown in Fig 3.10. This field configuration is such that the central tracking field is B_z=3.5T, while the field between the solenoids is B_z=-1.5T. The magnetic field of opposite sign in the air volume between the two solenoids will back-bend the muons for a very precise momentum measurement when compared with that obtainable within the flux return iron yoke of a traditional solenoid field. The basic element of the muon spectrometer is a proportional Al tube with a radius of 2.3 cm. The tube is filled with a gas mixture of 90% Helium - 10% Isobutane for a total drift time about 2 μs at the gain 10^5 readout the same technique of the cluster timing described in Section 1.2.

3.4.1 The Barrel and the EndCaps

The barrel part of the Muon Spectrometer consists of 3 staves, each containing 20 layers of tubes of 4 meters length. The three longitudinal staves have the corresponding drift tubes ganged together. Therefore, the total length of the barrel is 12 meters,covering the range of ± 45 degrees in θ. Each stave contains 6 sectors,one consisting of three basic modules that are bolted to-

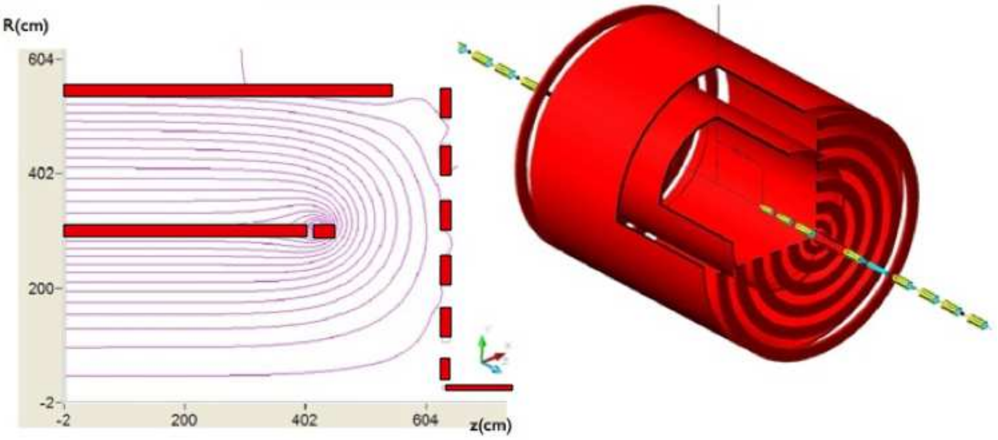

Figure 3.10: *The magnetic field configuration of the dual solenoids.*

gether to slide on appropriate rails on supports placed at the outer magnetic, as shown in Fig 3.12.

Each basic module contains 20 tubes radially and consists of either 460 or 1100 tubes for a total of 2020 tubes per side, summing to 12120 tubes per each of the three parts in which the full barrel is divided, for a total of 36360 tubes.

The endcaps have a dodecagonal shape, perfectly matching the front shape of the barrel. Each endcap is made of 3 planar sectors rotate by 120 degrees with respect to each other in order to have three independent projections, of 6 tubes each, as shown in Fig 3.13. Here also the drift tubes have maximum 4 meters length and, where this length is exceeded, the corresponding tubes are ganged togither. Each sector contains 1440 tubes so the total number of tubes in each endcaps is thus 4320. The total number of tubes in the Muon Spectrometer is 4500.

The high modularity of the detector assures, by mechanical constraints, a good positioning of the individual drift tubes, thus avoiding a very costly

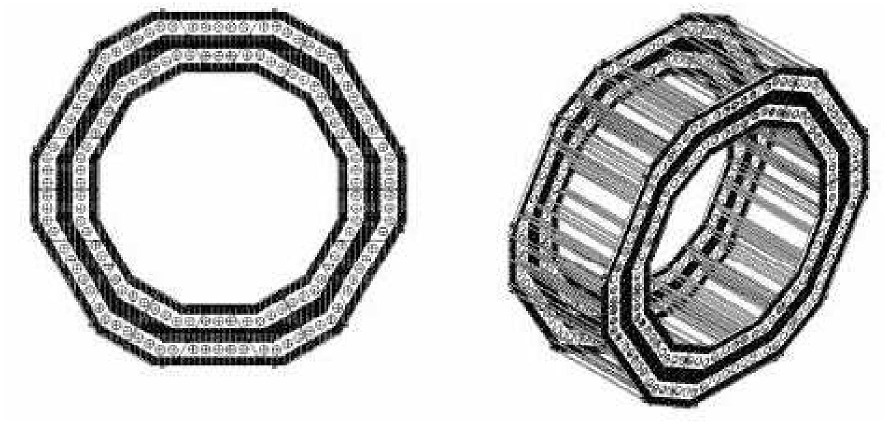

Figure 3.11: *Muon Spectrometer Barrel*

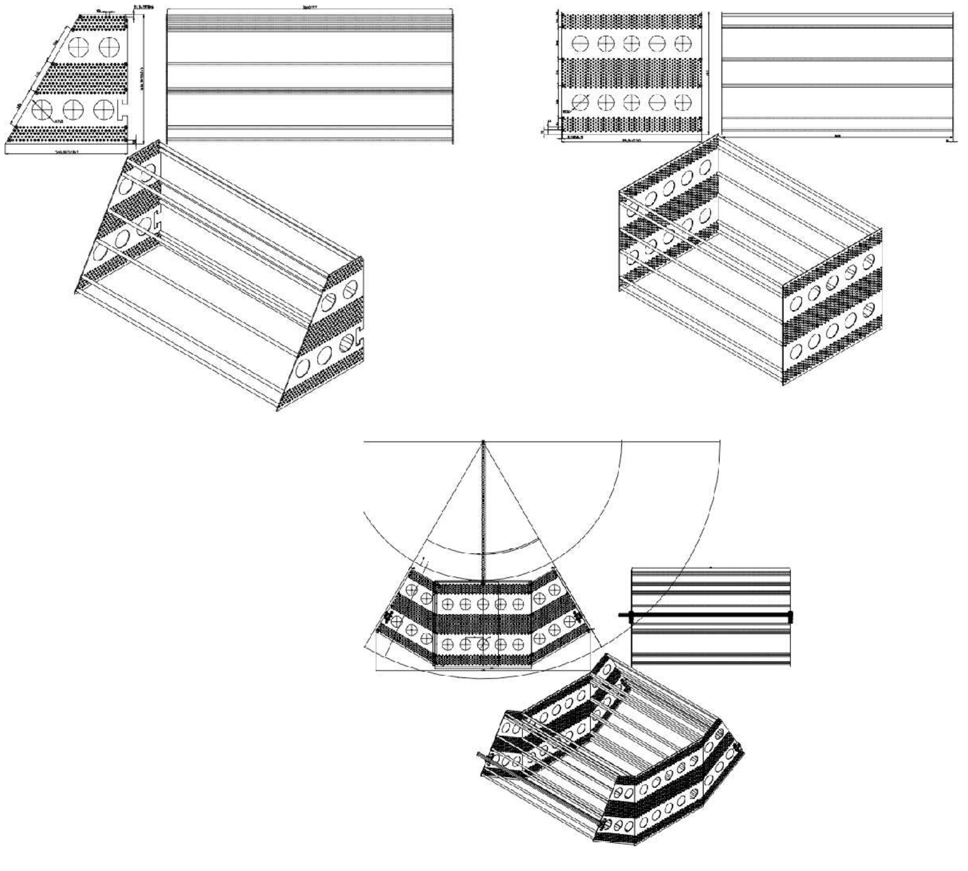

Figure 3.12: *Basic module Muon Spectrometer Barrel*

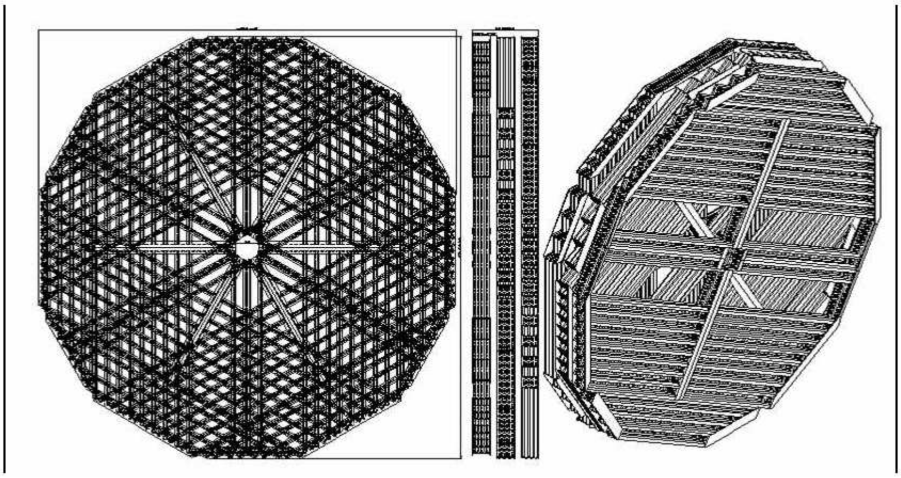

Figure 3.13: *Muon Spectrometer EndCap*

and complicated optical alignment system as in ATLAS.

3.4.2 Front end

The same CluCou chip is used as front end for the drift tubes. Here the longitudinal coordinate is given by current division, therefore the tubes are instrumented on both ends. High voltage and readout signals are distributed by using the same electronics card serving up to 25 tubes, thus preserving the high modularity of the system.

3.4.3 Muon Spectrometer Performances

Geometry Description

In the geometry class the MUD, I have implemented the algorithm to describe MUD geometry (cfr Sec 1.4.1). To build the MUD Barrel volume I have utilized, for every stave, two different basic volume with, respectively, a trapezoidal (TRD1) and a box (BOX) shape. Each stave volume consists of 6 sectors, obtained alternating TRD1 and two consecutive BOX shape. Each sector contais 20 layers of drift tubes, grouped in 5+10+5 layers (outer, middle, inner chamber) with air between their.

Detector Simulation

The simulations of the detectors volumes involved is quite accurate, including the thin walls of the straw tubes, the sense wires and the electronics. The support structures, however, have not been included. The simulation of the hits produced by the charged tracks in the MUD is handled by the Virtual Monte Carlo (VMC). The Digitization step is not implemented yet. The hits from the VMC are smeared according to a gaussian distribution with $\sigma_{r\Phi} = 200\mu$m and $\sigma_z = 3$mm, with the intent of simulating the readout of a proportional tube with charge division in the longitudinal direction. Random noise is, finally, added to the whole subdetector to simulate spurious hits.

Detector Reconstruction

The reconstruction in the MUD is performed by a Kalman Filter, cfr [15]. Only tracks that have already been reconstructed in DCH+VXD are extrapolated up to the inner layer the MUD and their parameters are estimated at the entrance of the Spectrometer. Fig 3.14 shows the transverse momentum resolution as function of the momentum for isolated muons reconstructed in the MUD, with momentum range, respectively of [0,200] and [0,20] GeV.
Fig 3.15 shows the transverse momentum resolution as function of θ. The efficiency is calculated for tracks that have been already reconstructed in CluCou. The cracks along the beam direction between the three staves of the detector(to accomodate the front-end electronics and the detector ser-

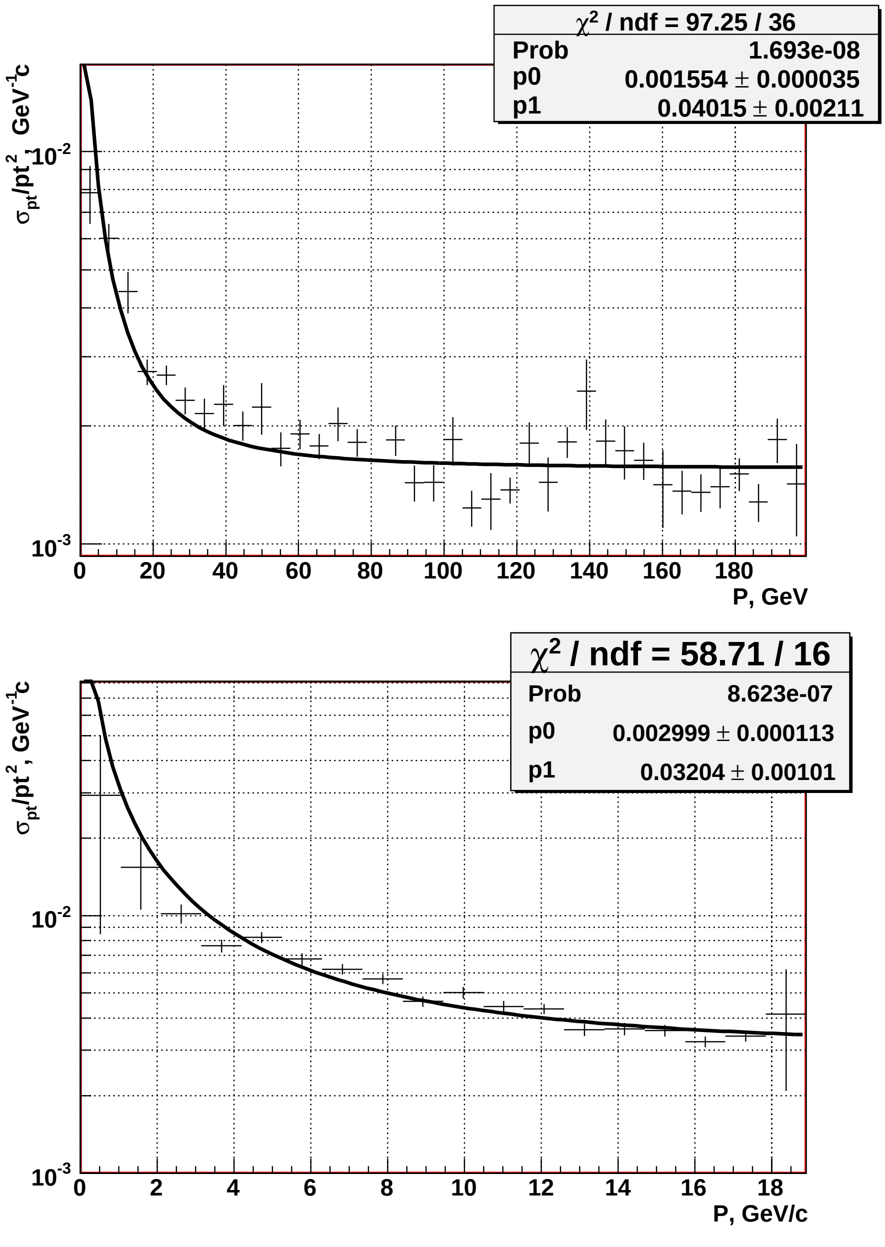

Figure 3.14: *Transverse momentum resolution as function of the momentum for isolated muons reconstructed in the MUD, with momentum range, respectively of [0,200] and [0,20] GeV*

vices) are clearly visible.

Finally, Fig 3.15 shows the reconstruction efficiency of the Global Tracker as a function of momentum for tracks not crossing the cracks of the MUD (namely $|\lambda| < 0.75$ and $|\lambda - 0.4| < 0.05$ with $\lambda = 90 - \theta$) that have been already reconstructed in CluCou.

In summary, the resolution of the Muon Spectrometer for is

$$\sigma(1/p_t) = 1.6 \times 10^{-3} \oplus 0.040/p_t \quad [Gev/c]^{-1}$$

The reconstruction efficiency of the tracker is 95% for muons with momentum above 6 GeV and not entering the cracks of the detector.

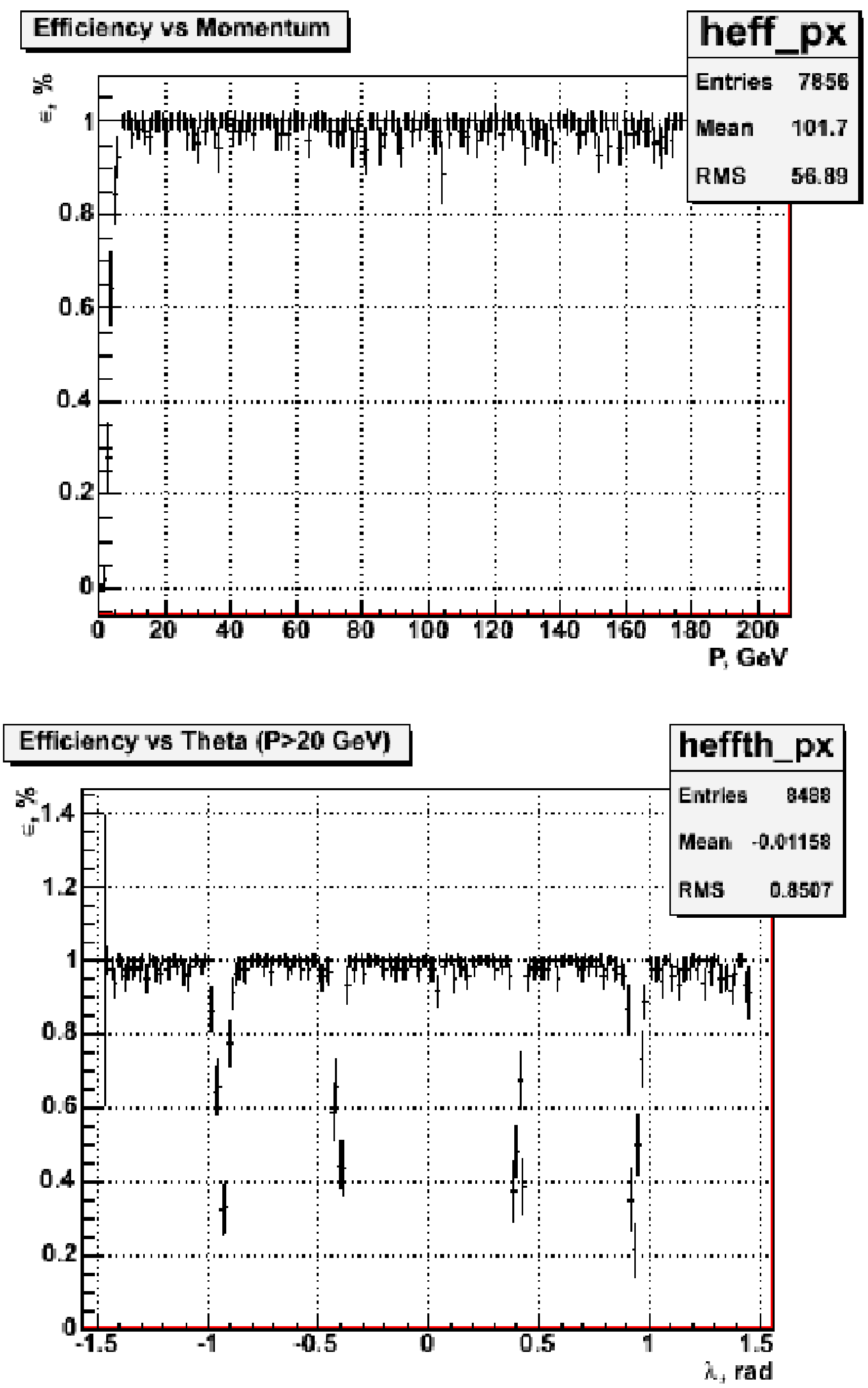

Figure 3.15: *Reconstruction efficiency as a function of the momentum for tracks not crossing the cracks of the Muon Spectrometer that have been already reconstructed in CluCou*

Chapter 4

Physics Results

4.1 Introduction

In this Chapter, some physics studies of the Higgs production in congiuction with a Z boson (Higgsstrahlung) are presented. In particular we consider the process $e^+e^- \rightarrow ZH \rightarrow \mu^+\mu^- + X$ and $e^+e^- \rightarrow ZH \rightarrow e^+e^- + X$, where the Z decay in a pair of charged leptons.

For this analysis, we have applied the recoil mass technique. The recoil mass analysis is an unbiased strategy to measure the Higgs mass, inclusively,

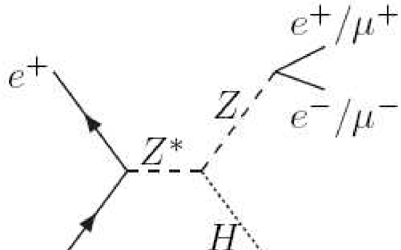

Figure 4.1: *Z^0 Feynman diagram of the Higgs-strahlung process*

by identifying and measuring the momentum of the two charged leptons in the final state. The Higgs mass is given by:

$$\begin{gathered} M_H^2 = E_H^2 - \vec{p}_H^{\,2} = (E_{CM} - E_Z)^2 - \vec{p}_Z^{\,2} \ , \\ E_Z = E_{l_1} + E_{l_2} \ , \quad \vec{p}_Z = \vec{p}_{l_1} + \vec{p}_{l_2} \end{gathered} \tag{4.1}$$

where E_Z and $\vec{p}_Z$ are, respectively, the energy and the momentum of the Z boson and l_i are the leptons in the final state. Higgs mass resolution depends on the momentum resolution of the tracking system in the case of $\mu^+\mu^-$, and on the combined calorimeter and tracking system resolution in the case of e^+e^-. In both cases, particle identification is required to tag the final state and to reject, for example, single $\pi^\pm$ from τ decay as background. The figure-of-merit of such analysis is the accuracy and the resolution on the Higgs mass.

Another relevant issue to the presented analyses is the polarization of the electron and positron beams. We have decided to perform these physics studies in the most conservative configuration of an electron beam with 100% left-handed polarization and a positron beam with 100% right-handed polarization in order to maximize the WW background.

Because the impact of background induced by beam-pairs is negligible in 4th Concept (due to the fact that our central tracker integrates only one bunch crossing and the process of track finding is performed mostly in that detector), in the first phase of the physics studies, we have decide to neglect the effects of beam-pair beckground.

The signal and background samples have been generated at DESY by the ILD collaboration. The simulation codes use Fluka and Whizard inside ILCRoot (Sez. 2.4) over the full 4th detector.

4.2 Analysis of $e^+e^- \rightarrow ZH \rightarrow \mu^+\mu^- + X$ at Ecms=250 GeV

4.2.1 Detector challenges

Two sub-systems are particularly challenged by this event topology: the tracking systems and the muon spectrometer. The proposed central tracking system, CluCou (Sec. 3.3), is optimized to minimize, the multiple scattering contribution to the momentum measurement, particularly for momenta below 30 GeV/c. At higher momenta, the use of the cluster counting technique guarantees good spatial resolution and, therefore, good momentum resolution, which is of most importance for the analysis. In this analysis, the Muon Spectrometer is used as a Particle Identifier to select the muons from the decay of the Z boson.

4.2.2 Event Simulation

At ILC, beamstrahlung and Initial State Radiation (ISR), may be not negligible so that, event by event, the E_{CM} is spread around its nominal value ($\tilde{E}_{CM}$). In the simulation, we have token into account such effects. The Higgs has been simulated with a mass of 120 GeV/c^2, and negligible width. The CM energy has been chosen near the production threshold, $\tilde{E}_{CM} = 250$ GeV, where a large Higgsstrahlung cross section is expected. The beam spread used in the simulation for both the electron and positron beams corresponds to an initial beam energy spread of 0.3%.

4.2.3 Physics background

The expected dominant background is due to the production of two Z boson of which at least one Z decays into two muons: $e^+e^- \rightarrow ZZ \rightarrow \mu^+\mu^- + X$. The expected number of events is $\simeq 7$ times that of the signal. This background is almost irreducible, carrying the exact same topology as the signal and it can be rejected only according to the recoil mass. The second kind of background, also expected to be large, is due to the process $e^+e^- \rightarrow \mu^+\mu^-\nu\overline{\nu}$, which occurs mostly trough the production of two W bosons. Other two relevant sources of background, considered for this analysis are: $e^+e^- \rightarrow \mu^+\mu^-$ and $e^+e^- \rightarrow \mu^+\mu^-\mu^+\mu^-$. In principle, the topology of these reactions is quite different from the signal, as the two muons do not come from the decay of a Z boson and the remaining particles are not associated to a Higgs boson. However, the huge cross section of these background channels (17.1 pb and 11.4 fb respectively) are order of magnitude larger than the signal (about 17.1 fb). Therefore, combinatorics could easily feed background events into the sample selected for analysis. In order to overcome the large amount of events corresponding to the cross sections of the two background channels considered, we have performed an initial screening of the generated sample and retained for further analysis only those events surviving the set of kinematic conditions listed below:

1. $|cos\theta_\mu| < 0.98$
2. $P_t(\mu^\pm) > 9\ GeV/c$
3. $72 < M(\mu^+\mu^-) < 110.4\ GeV/c^2$
4. $102 < M_{recoil}(\mu^+\mu^-) < 168\ GeV/c^2$
5. At least 2 charged tracks for the $e^+e^- \rightarrow \mu^+\mu^-$ Montecarlo sample

6. At least 4 charged tracks for the $e^+e^- \to \mu^+\mu^-\mu^+\mu^-$ Montecarlo sample

Final state	$P_t(\mu^\pm) > 3.5 GeV$	$P_t(\mu^\pm) > 9 GeV$	$P_t(\mu^\pm) > 12 GeV$
$e^+e^- \to ZH \to \mu^+\mu^- + X$	96.2%	94.2%	93.8%
$e^+e^- \to \mu^+\mu^-$	8.5%	8.3%	8.1%
$e^+e^- \to \mu^+\mu^-\mu^+\mu^-$	16.1%	16.1%	16.1%
$e^+e^- \to \mu^+\mu^-\tau^+\tau^-$	18.0%	17.7%	17.6%
$e^+e^- \to \mu^+\mu^-e^+e^-$	1.7%	1.3%	1.2%
$e^+e^- \to \mu^+\mu^-\nu\overline{\nu}$	14.1%	13.8%	13.6%
$e^+e^- \to \mu^+\mu^-u\overline{u}$	19.7%	19.3%	19.2%
$e^+e^- \to \mu^+\mu^-d\overline{d}$	20.7%	20.2%	20.0%
$e^+e^- \to \mu^+\mu^-s\overline{s}$	21.0%	20.7%	20.5%
$e^+e^- \to \mu^+\mu^-c\overline{c}$	19.5%	19.3%	19.1%
$e^+e^- \to \mu^+\mu^-b\overline{b}$	21.7%	21.0%	20.9%

Table 4.1: *Fraction of signal and background events surviving the preliminary cuts for different values of the transverse momentum cut.*

The fraction of signal and background events surviving these preliminary cuts is shown in table 4.1 for various values of the tansverse momentum cut. Other possible source of background for this channel is $e^+e^- \to \tau^+\tau^-$. A quick test, however, shows that the probability for these events to survive the selection chain is negligible and we have decided to skip this background source in the analysis. After the precuts, the events are reconstructed according to the flow described in sec. 2.4. The combined precut and reconstruction efficiency for $e^+e^- \to ZH \to \mu^+\mu^- + X$ events is 90.6%. This number includes a geometric efficiency and a reconstruction efficiency of 96.1%.

4.2.4 Strategy of the analysis

The signature of the signal events for this channel are two high energy muon tracks with a common vertex compatible with the interaction point. The invariant mass of the two muon system must be near the Z mass. The set of cuts described in sec. 4.2.3 is replicated on the reconstructed particles.

The second step in this analysis is to identify and reconstruct events with exactly two muons that have survived the cuts. We do that by imposing that the tracks reconstructed by the central tracker are successfully prolongated and reconstructed by the Kalman filter in the Muon Spectrometer (μID). We also require that the distance of closest approach to the origin for each candidate muon be less than 6mm (DCA<6mm). This cut will reject the non prompt muons likely produced by long lived, semi-leptonic weak decays. We also require that μ momenta are both above 20 GeV/c ($P_\mu > 20\, GeV/c$). The total efficiency for the signal events to survive the double muon-ID selection is 80.5%. The 19.5% inefficiency is due to the cracks in the Muon Spectrometer. The fraction of surviving events is 72.9% with purity of the selection corresponding to 99.99%. The fraction of background events surviving the muon-ID selection corresponds to 80.37%. However, additional cuts are necessary to reject the background related to $e^+e^- \to \mu^+\mu^-$, $e^+e^- \to \mu^+\mu^-\nu\overline{\nu}$ and $e^+e^- \to \mu^+\mu^-\mu^+\mu^-$ events. Such events have, low track multiplicity and their topology is incompatible with the presence of a Higgs boson in the final state. Therefore, we apply the following topological cut to the signal and background samples which passed the muon-Id requirements:

1. At least 5 charged tracks successfully reconstructed (including the muons)

The cut on the minimum number of reconstructed tracks rejects 12.1% of the signal (mostly due to tracking inefficiencies because of absence of a standalone muon reconstruction algorithm) almost entirely due to the Higgs decays into 2 τ lepton. We decided to apply it any way for the sake of a cleaner final sample. The fraction of signal and background events surviving these cuts are summarized in table 4.2:

Final state	Fraction of Surviving events
$\mu\mu X$	87.9%
background	13.6%

Table 4.2: *Fraction of signal and background events surviving the additional cuts.*

Other possible cuts would be essentially aimed at a further rejection of the large $e^+e^- \rightarrow \mu^+\mu^-$ with an ISR or breemsstrahlung photon. However, no further cuts are applied to the signal and background sample as we believe that the signal to noise ratio obtained is large enough to allow a good measurement of the recoil mass without affecting the statistics of the sample. This is also true for the Standard Model background: $e^+e^- \rightarrow ZZ \rightarrow \mu^+\mu^- + X$. Infact, the good momentum and energy resolutions of the 4th Concept detector allows for a clear separation of the invariant masses of the Z and H bosons (for a mass of 120 GeV/c^2) in the recoil mass spectrum with no need to remove part of the background (and signal) with dedicated cuts. Total fraction of signal and background events surviving all the cuts is summarized in Table 4.3

Final state	Fraction of Surviving events
$\mu\mu X$	64.1%
background	8.2%

Table 4.3: *Total fraction of signal and background events surviving all the cuts.*

4.2.5 Results

The reconstruction of the Z boson, decaying into two muons, is done by selecting, among all the reconstructed muons, the $\mu^+ - \mu^-$ pair that gives a Z invariant mass nearest to the Z mass value. The resolution on the muon momentum is shown in fig. 4.2 and correspond to about 80 MeV/c, with some tail.

In fig. 4.3 and 4.4 we show the mass resolution for the invariant mass for the two muons and for the recoil systems. The plots show the difference between the generated and the reconstructed values.

Finally,in fig. 4.5 and 4.6, we show the recoil mass distribution for the process $e^+e^- \rightarrow ZH \rightarrow \mu^+\mu^- + X$ along with the described backgrounds for M_H= 120 GeV/c^2 and 500 fb^{-1} at ILC with E_{CM}=250 GeV. The red histogram corresponds to the signal, the black histgram to the background while the blue curve is the sum of the two contributions.

We fit the Higgs boson mass described by the same parametrization used in reference [34] to the spectra shown in Figure 4.5. The background originating from the SM processes described in setion 4.2.3 is parametrised by a second order polynomial whose coefficients are allowed to vary in the fit. Finally, we can see that, with the momentum resolution of the 4th Concept drift

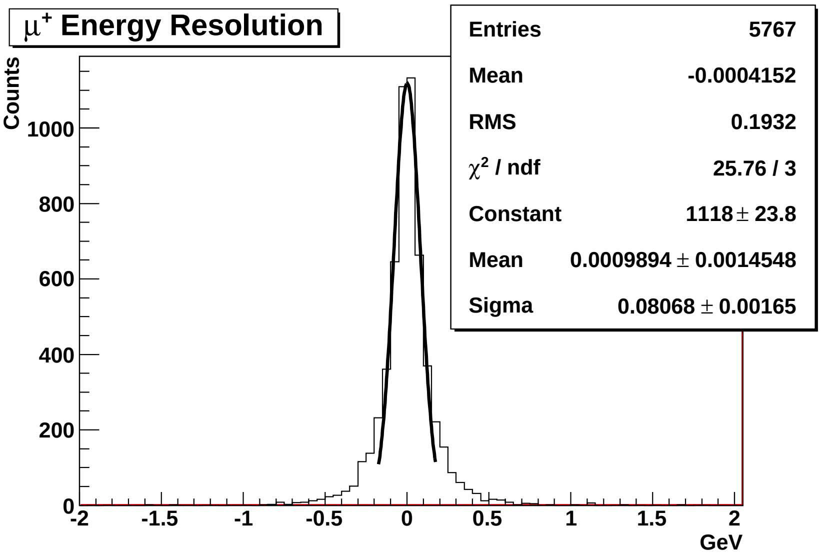

Figure 4.2: *Momentum resolution of the muons reconstructed by a Kalman fit using the Vertex Detector, the Drift Chamber and the Muon Spectrometer.*

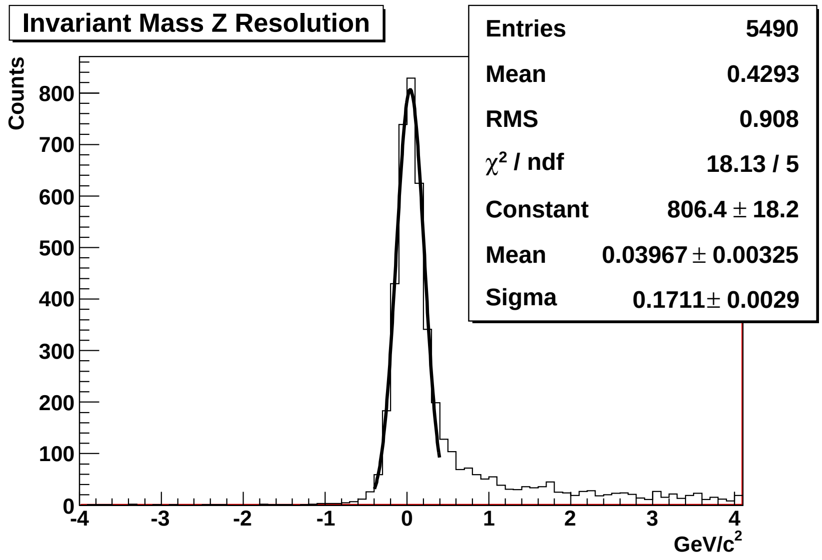

Figure 4.3: *Z boson invariant mass resolution in the process* $e^+e^- \rightarrow ZH \rightarrow \mu^+\mu^- + X$ *for* M_H= *120 GeV/*c^2 *and 500* fb^{-1} *at ILC with* E_{CM}*=250 GeV.*

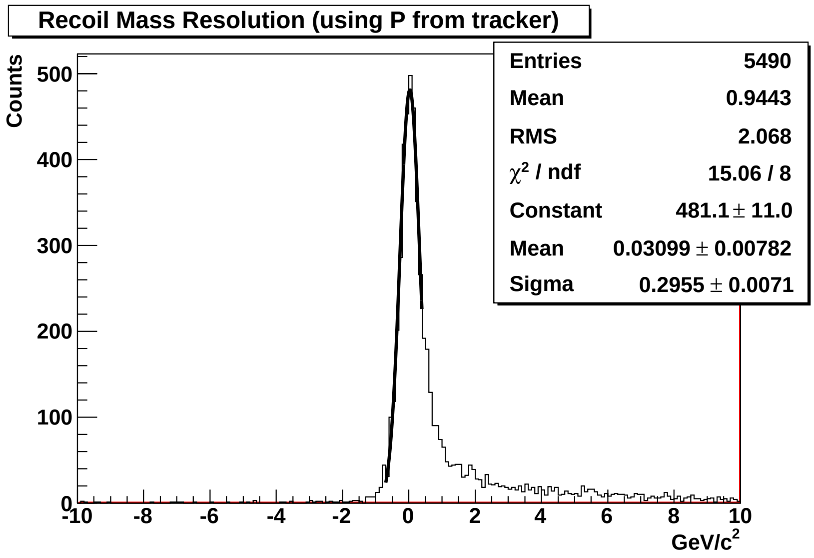

Figure 4.4: *Recoil mass resolution in the process* $e^+e^- \rightarrow ZH \rightarrow \mu^+\mu^- + X$ *for* M_H= *120* GeV/c^2 *and 500* fb^{-1} *at ILC with* E_{CM}=*250* GeV.

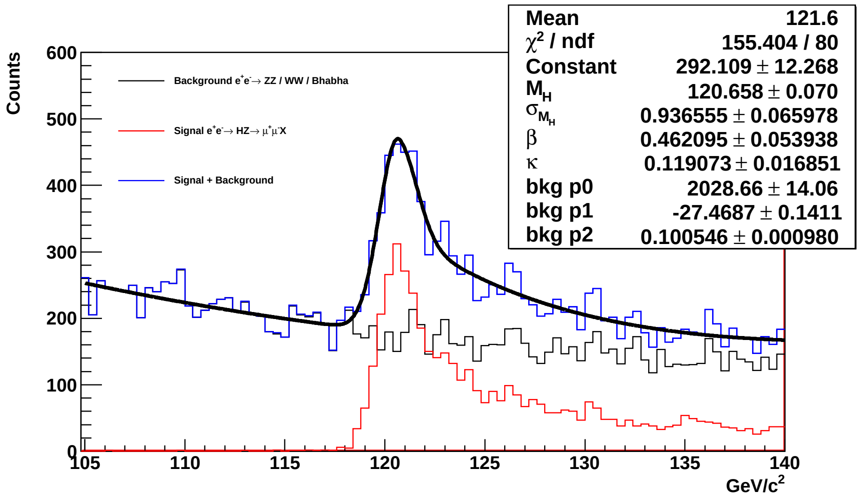

s

Figure 4.5: *Recoil mass distribution for the process* $e^+e^- \rightarrow ZH \rightarrow \mu^+\mu^- + X$ *along with the described backgrounds for* M_H= *120* GeV/c^2 *and 500* fb^{-1} *at ILC with* E_{CM}=*250* GeV.

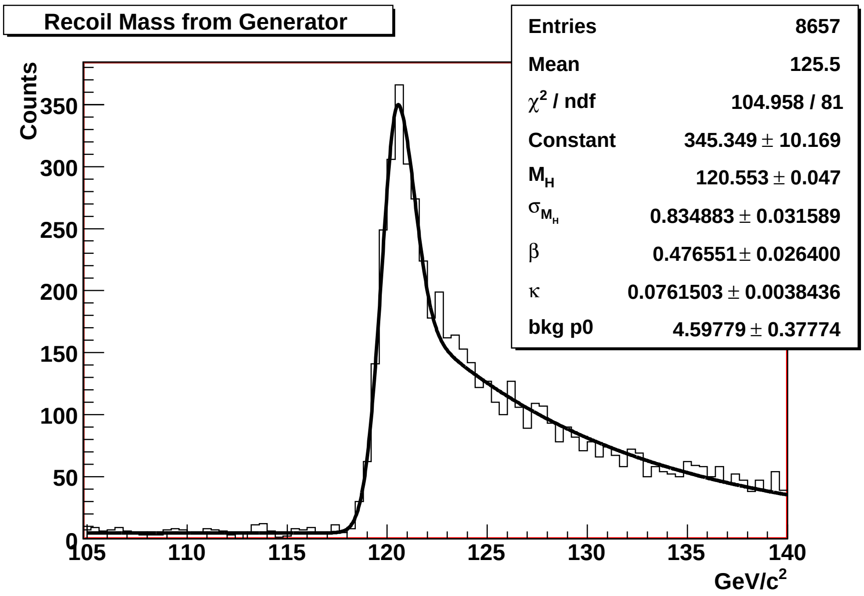

Figure 4.6: *Recoil mass distribution as generated by Whizard for the process* $e^+e^- \rightarrow ZH \rightarrow \mu^+\mu^- + X$ *for* M_H= *120 GeV/*c^2 *and 500* fb^{-1} *at ILC with* E_{CM}*=250 GeV.*

chamber combined with the vertex detector, the Z mass is reconstructed with a precision of $\lesssim 170$ MeV/c^2 (cfr. Fig. 4.3) and the Higgs is reconstructed with a $\sigma \simeq 937$ MeV/c^2 and a systematic shift of $\simeq 660$ MeV/c^2, 550 MeV/c^2 of which due to fluctuation of the center of mass energy (Fig. 4.5, 4.6).

Cross section measurement

The mass spectra in Figure 4.5 is used to determine the cross sections for the process $e^+e^- \to ZH \to \mu^+\mu^- + X$.

$$\sigma = \frac{1}{\epsilon_{sel}} \left(\frac{N_{Signal}}{L} \right) \tag{4.2}$$

while the uncertainty is calculated as

$$(\Delta\sigma)^2 = \sigma^2 \left[\left(\frac{\Delta\epsilon_{sel}}{\epsilon_{sel}} \right)^2 + \frac{1}{N_{Signal}} + \left(\frac{\Delta L}{L} \right)^2 \right] \tag{4.3}$$

where:

- N_{Signal} is the integral over the red histogram of fig. 4.5
- ϵ_{sel} is the selection efficiency
- L is the luminosity

By inserting in the formula the results obtained from the fit in fig. 4.5 we get a cross section of 13.62 ± 2.12 fb

4.3 Analysis of $e^+e^- \to ZH \to e^+e^- + X$ at Ecms=250 GeV

The Higgs-strahlung process with the Z decaying into electron pairs is very similar to the case discusses in section 4.2. However, there are two main differences related to the analysis of the signal and the background. Regarding the signal, we need to take into account the situation where at least one of the electrons from the Z boson decay emits a photon by breemsstrahlung. Neglecting such photons would cause a distortion in the lineshape of the Z boson mass which would reflects into a shoulder in the recoil mass spectrum. The second difference is that a major background for this channel is from the large number Bhabha events that could possibly feed into the events selected for analysis by combinatorics. Therefore, we have applied to the analysis presented in section 4.2 appropriate modifications to take into account these issues. The event simulation for the $e^+e^- \rightarrow ZH \rightarrow e^+e^- + X$ reaction is similar to that described for the $e^+e^- \rightarrow ZH \rightarrow \mu^+\mu^- + X$ reaction in section 4.2.2.

4.4 Physics background

The expected dominant background is due to the production of two Z boson, of which at least one Z decays into two electrons: $e^+e^- \rightarrow ZZ \rightarrow e^+e^- + X$. This background is almost irreducible, carrying the exact same topology as the signal and it can be disentangled only via an appropriate fit to the lineshape of the Z and H bosons. The second kind of background, also expected to be large, is due to the process $e^+e^- \rightarrow e^+e^-\nu\overline{\nu}$, which occur mostrly trough the production of two W bosons, especially in the case considered here with both beams fully polarized. Other two relevant sources of background, considered for this analysis are: $e^+e^- \rightarrow e^+e^-$ and $e^+e^- \rightarrow e^+e^-e^+e^-$. In principle, the topology of these reactions is quite different from the signal, as the two electrons do not come from the decay of a Z boson and the remaining particles are not associated to a Higgs boson. However, the huge cross section of these background channels (17.3 nb and 1.1 pb respectively) are order of magnitude larger than the signal (about 17.9 fb). Therefore, combinatorics could easily feed background events into the sample selected for analysis. This is especially true in the case of a radiative photon that converts into an extra electron-positron pair. In order to overcome the large amount of events corresponding to the cross sections of the two background channels considered, we have performed an initial screening of the generated sample and retained for further analysis only those events surviving the set of kinematic conditions listed below:

1. $|cos\theta_e| < 0.95$
2. $P_t(e^{\pm}) > 9\ GeV/c$
3. $72 < M(e^+e^-) < 110.4\ GeV/c^2$
4. $102 < M_{recoil}(e^+e^-) < 168\ GeV/c^2$
5. At least 2 charged tracks for the $e^+e^- \rightarrow e^+e^-$ Montecarlo sample
6. At least 4 charged tracks for the $e^+e^- \rightarrow e^+e^-e^+e^-$ Montecarlo sample

The fraction of signal and background events surviving these preliminary cuts is shown in table 4.4 for various values of the tansverse momentum cut.

Another possible source of background for this channel is $e^+e^- \rightarrow \tau^+\tau^-$. Also in this case, a quick test shows that the probability for these events to survive the selection chain is negligible and we have decided to skip this background source in the rest of the analysis. After the precuts, the events are reconstructed according to the flow described for the previous analysis. The combined precut and reconstruction efficiency for $e^+e^- \rightarrow ZH \rightarrow e^+e^- + X$ events is 87.5%. This number includes a combined geometric efficiency

Final state	$P_t(e^{\pm}) > 3.5\ GeV$	$P_t(e^{\pm}) > 9\ GeV$	$P_t(e^{\pm}) > 12\ GeV$
Hee	95.9%	93.2%	91.2%
$e^+e^- \to e^+e^-$	0.24%	0.047%	0.028%
$e^+e^- \to e^+e^-e^+e^-$	2.7%	1.9%	1.7%
$e^+e^- \to e^+e^-\tau^+\tau^-$	2.14%	0.94%	0.81%
$e^+e^- \to e^+e^-\mu^+\mu^-$	1.97%	0.71%	0.58%
$e^+e^- \to e^+e^-\nu\overline{\nu}$	14.9%	13.9%	13.4%
$e^+e^- \to e^+e^-u\overline{u}$	4.4%	3.4%	2.7%
$e^+e^- \to e^+e^-d\overline{d}$	12.4%	10.9.2%	10.5%
$e^+e^- \to e^+e^-s\overline{s}$	12.5%	11.0%	10.6%
$e^+e^- \to e^+e^-c\overline{c}$	4.3%	3.4%	2.7%
$e^+e^- \to e^+e^-b\overline{b}$	14.2%	13.1%	12.9%

Table 4.4: *Fraction of signal and background events surviving the preliminary cuts for different values of the transverse momentum cut.*

and a reconstruction efficiency of 93.8%. The set of cuts described in sec. 4.4 is replicated on the reconstructed particles.

4.4.1 Strategy of the analysis

The signature of the signal events for this channel are two high energy electron tracks with a common vertex compatible with the interaction point. The invariant mass of the two electron system must be near the Z mass.

The second step in this analysis is to identify and reconstruct events with exactly two electrons that have survived the cuts described previously in Sec.

4.4). We do that by using the following strategy:

1. We first extrapolate the candidate electron track to the electromagnetic calorimeter and look for an associated shower.

2. The energy of this shower must be compatible with the momentum of the track measured by the tracking system.

3. If the match is poor, we extrapolate the shower axis into the hadronic calorimeter. If an energy deposit is found, it must be smaller than 20% of the corresponding energy measured in the electromagnetic calorimeter

4. Finally, the *Čerenkov* and *Scintillation* components of the shower must be consistent with an electron hypothesis. More specifically, we make the following requirement:

$$\frac{E_{Sc} - E_{cer}}{E_{Sc} + E_{Ce}} < 6 \ \times \sigma_{calib} \tag{4.4}$$

   where σ_{calib} corresponds to the the width of the distribution obtained during the calibration of the calorimeter.

The total efficiency for the signal events to survive the double electron-ID selection is 81.7% (corresponding to 93.4% of the events successfully reconstructed by the Kalman filter). The purity of the signal (namely, the fraction of events with two electrons correctly identified) is 98.2%. The fraction of background events surviving the electron-ID selection corresponds to 76.1%.

However, additional cuts are necessary to reject the background related to $e^+e^- \rightarrow e^+e^-$, $e^+e^- \rightarrow e^+e^-\nu\overline{\nu}$ and $e^+e^- \rightarrow e^+e^-e^+e^-$ events. Such events have low track multiplicity and their topology is incompatible with the presence of a Higgs boson in the final state. Therefore, we apply the following topological cuts to the signal and background samples which passed the electron-Id requirements:

1. $P_e > 20\ GeV/c$
2. At least 5 charged tracks successfully reconstructed
3. Distance of closest approach to the origin for the candidate electron tracks $<$ 6 mm.

The cut on the minimum number of reconstructed tracks rejects only 4.8% of the signal, almost entirely due to the Higgs decays into 2 τ lepton. The fraction of signal and background events surviving these cuts are summarized in table 4.5:

Final state	Fraction of Surviving events
e^+e^-X	95.2%
background	13.15%

Table 4.5: *Fraction of signal and background events surviving the additional cuts.*

Other possible cuts would be essentially aimed at a further rejection of the large $e^+e^- \rightarrow e^+e^-$ with an ISR or breemsstrahlung photon. However, no further cuts are applied to the signal and background sample as we believe that the signal to noise ratio obtained is large enough to allow a good measurement of the recoil mass without affecting the statistics of the sample. This is also true for the Standard Model background: $e^+e^- \rightarrow ZZ \rightarrow e^+e^- + X$. Infact, the good momentum and energy resolutions of the 4th Concept detector allows for a clear separation of the invariant masses of the Z and H bosons, in the recoil mass spectrum with no need to remove part of the background (and signal) with dedicated cuts. The total fraction of signal and background events surviving all the cuts is summarized in the table 4.6

Final state	Fraction of Surviving events
e^+e^-X	68.3%
background	4.4%0.0015%

Table 4.6: *Total fraction of signal and background events surviving all the cuts.*

4.4.2 Results

The reconstruction of the Z boson, decaying into two electrons, is done by selecting, among all the reconstructed electrons, the $e^+ - e^-$ pair that gives a Z invariant mass nearest to the Z mass value. In the case of presence of a bremsstralung photon, the 4-momentum of the combined e-γ pairs is obtained by combining the tracking informations with those obtained from the electromagnetic calorimeter. Otherwise, the momentum of the electron is obtained by the tracking systems only. The resolution on the electron momentum is shown in fig. 4.7 when it is reconstructed by the tracking systems and in fig. 4.8 when the electromagnetic calorimeter is also used.

The electron energy resolution is about 80 MeV in the first case (as in the muon case) and about 190 MeV in the second case.

In fig. 4.9 and 4.10 we show the Z invariant mass resolution in the case of particles reconstructed in the tracking systems or in the calorimeter. Similarly, in fig. 4.11 and 4.12 we show the mass resolution for the recoil system

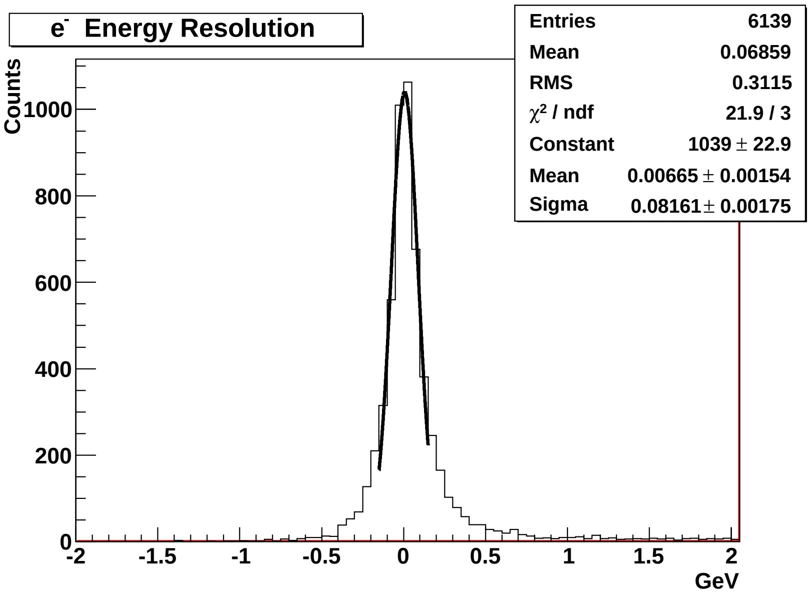

Figure 4.7: *Momentum resolution of the electrons reconstructed by a Kalman fit using the Vertex Detector and the Drift Chamber.*

for both cases. The plots show the difference between the reconstructed and generated values.

Finally, in fig. 4.13 and 4.14 we show recoil mass distribution for the process $e^+e^- \to ZH \to e^+e^- + X$ along with the described background for M_H= 120 GeV/c^2 and 500 fb^{-1} at ILC with E_{CM}=250 GeV with the electrons reconstructed, respectively, using the tracking systems only and in combination with the electromagnetic calorimeter. The red histogram corresponds to the signal, the black histgram to the background while the blue curve is the sum of the two contributions.

The same fitting technique is performed as for the $\mu^+\mu^-$ case [34].

The background originating from the SM processes described in setion 4.4 is parametrised by a second order polynomial whose coefficients are allowed to vary in the fit. Finally, we can see that with the momentum resolution

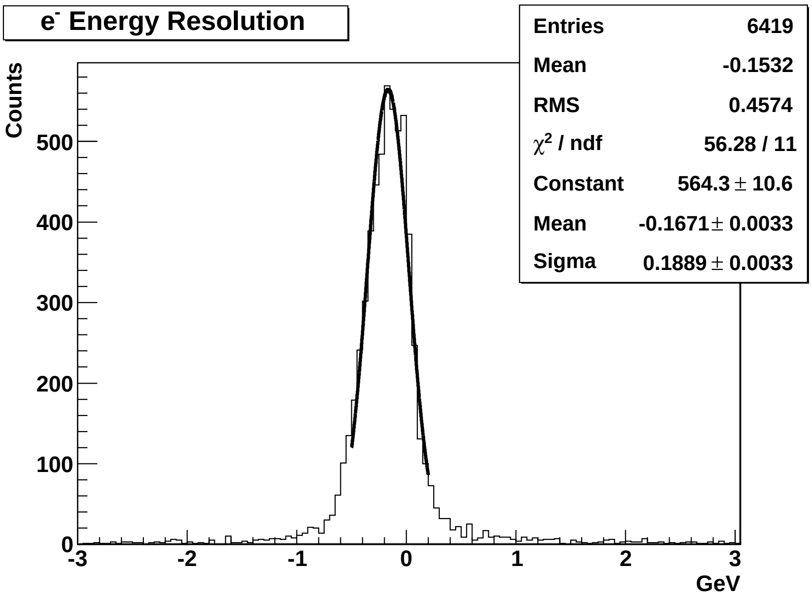

Figure 4.8: *Momentum resolution of the electrons reconstructed in the tracking systems and in the electromagnetic calorimeter.*

of the 4th Concept drift chamber combined with the vertex detector the Z mass is reconstructed with a precision of $\lesssim$ 150 MeV/c^2 when the electron is reconstructed in the tracking system (cfr Fig. 4.9) and $\lesssim$ 274 MeV/c^2 in the case of the electrons and breemsstrahlung photon are reconstructed also using the electromagnetic calorimeter(cfr. fig. 4.9). In the latter case, however, the long tails due to the breemsstrahlung photons are no longer present in the distribution. Similarly, the Higgs mass can be reconstructed with a $\sigma \simeq$ 400 MeV/c^2 in the case of pure tracking reconstruction (cfr Fig. 4.11) and $\sigma \simeq$ 430 MeV/c^2 in the case of combined reconstruction (cfr Fig. 4.12). We observe that, in spite of being about 30 MeV/c^2 larger, the plot obtained from the combined tracking and calorimetric informations is actually cleaner, with no tails from unreconstructed breemsstrahlung photons.

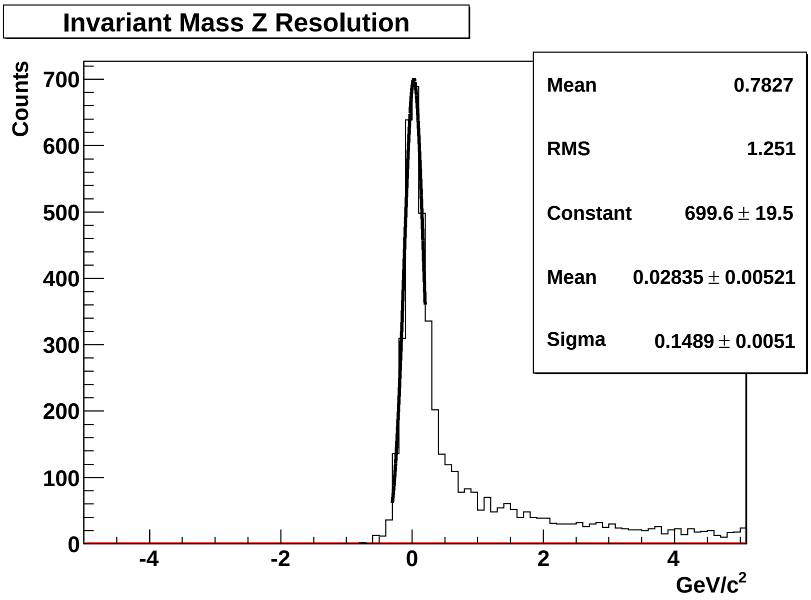

Figure 4.9: *Z boson invariant mass resolution distribution in the process $e^+e^- \rightarrow ZH \rightarrow e^+e^- + X$ for M_H= 120 GeV/c^2 and 500 fb^{-1} at ILC with E_{CM}=250 GeV with the electrons reconstructed in the tracking systems only.*

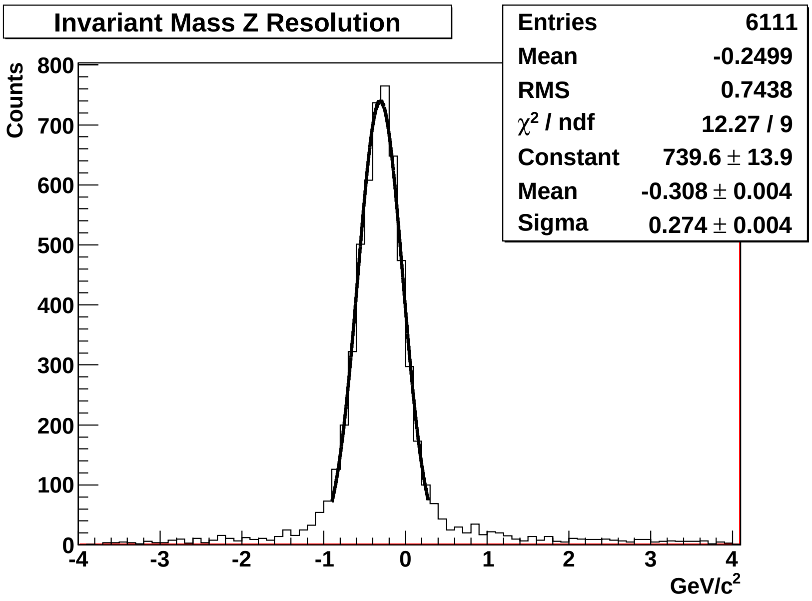

Figure 4.10: *Z boson invariant mass resolution distribution in the process* $e^+e^- \rightarrow ZH \rightarrow e^+e^- + X$ *for* M_H= *120 GeV/*c^2 *and 500* fb^{-1} *at ILC with* E_{CM}=*250 GeV with the electrons and the accompanying breemsstralung photon reconstructed in the tracking systems and in the calorimeter.*

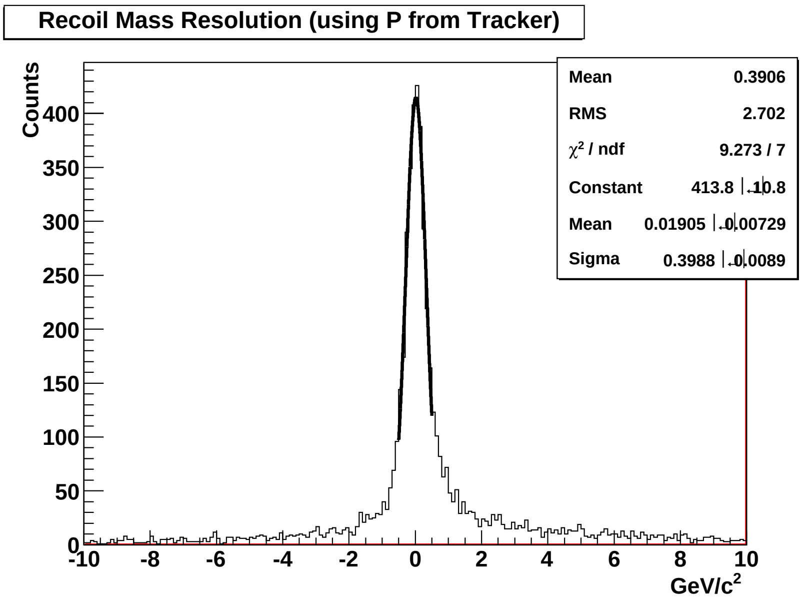

Figure 4.11: *Recoil mass resolution in the process* $e^+e^- \rightarrow ZH \rightarrow e^+e^- + X$ *for* M_H= *120 GeV/*c^2 *and 500* fb^{-1} *at ILC with* E_{CM}*=250 GeV with the electrons reconstructed in the tracking systems only.*

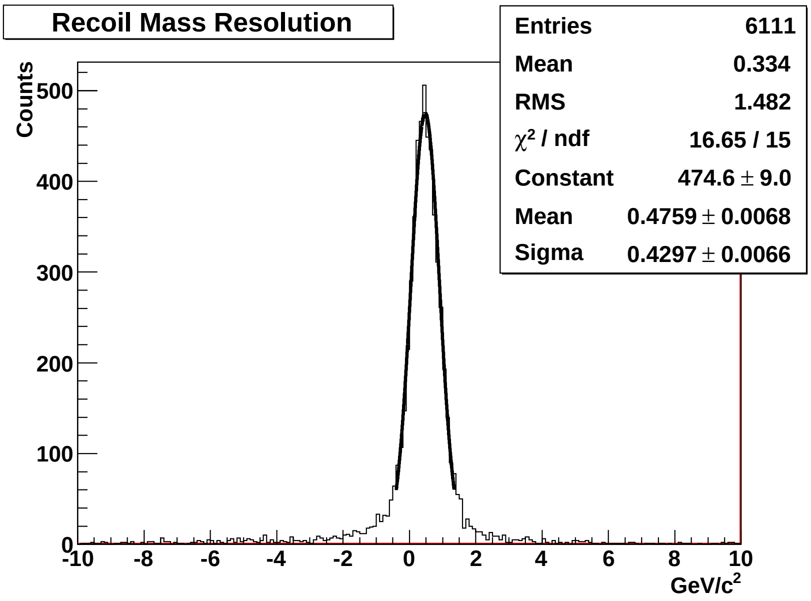

Figure 4.12: *Recoil mass resolution in the process* $e^+e^- \to ZH \to e^+e^- + X$ *for* M_H= *120 GeV/*c^2 *and 500* fb^{-1} *at ILC with* E_{CM}*=250 GeV with the electrons and the accompanying breemstrahlung photon reconstructed in the tracking systems and in the calorimeter.*

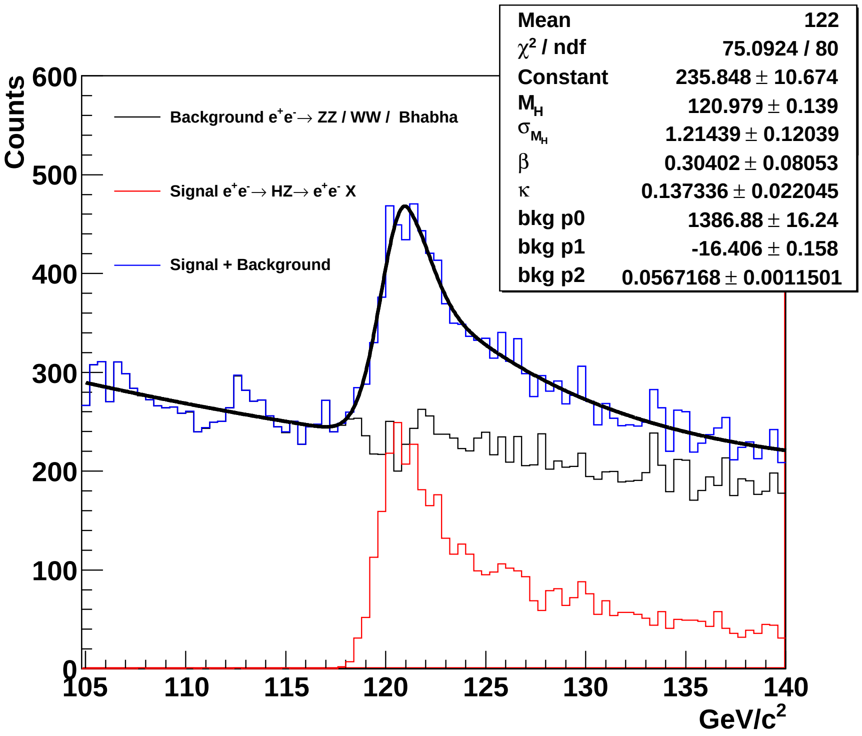

Figure 4.13: *Recoil mass distribution for the process* $e^+e^- \longrightarrow ZH \longrightarrow e^+e^- + X$ *along with the background for* M_H= *120 GeV/*c^2 *and 500 fb*$^{-1}$ *at ILC with* E_{CM}=*250 GeV with the electrons reconstructed in the tracking systems only.*

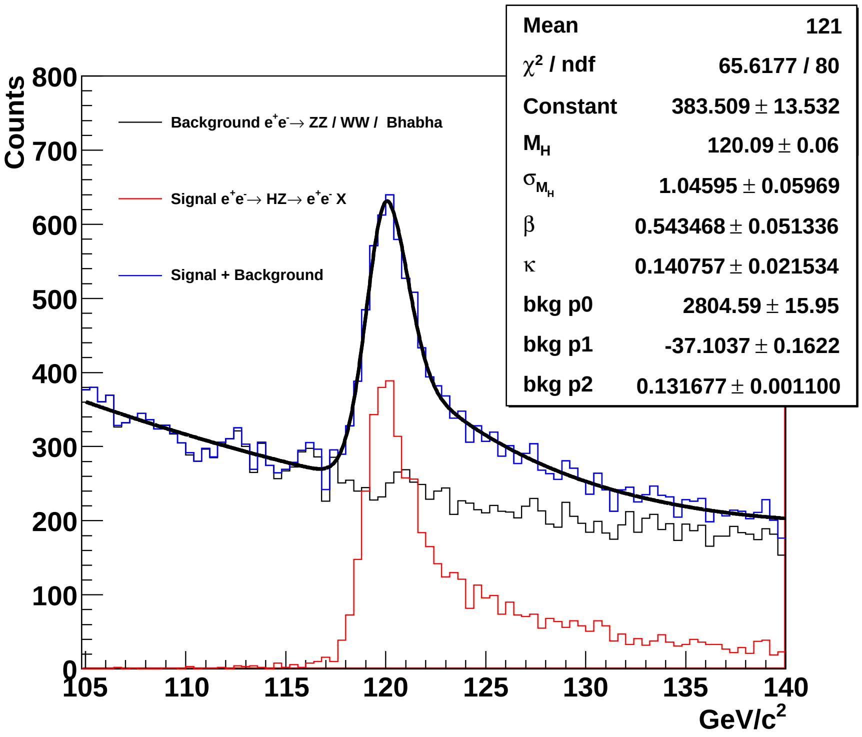

Figure 4.14: *Recoil mass distribution for the process* $e^+e^- \longrightarrow ZH \longrightarrow e^+e^- + X$ *along with the background for* M_H= *120 GeV/*c^2 *and 500* fb^{-1} *at ILC with* E_{CM}*=250 GeV with the electrons reconstructed in the tracking systems and in the calorimeter.*

Cross section measurement

The mass spectrum in Figures 4.13 and 4.14 are used to determine the cross sections for the process $e^+e^- \to ZH \to e^+e^- + X$ We use the same formulas as in the $\mu^+\mu^-$:

$$\sigma = \frac{1}{\epsilon_{sel}} \left(\frac{N_{Signal}}{L} \right) \tag{4.5}$$

while the uncertainty is calculated as

$$(\Delta\sigma)^2 = \sigma^2 \left[\left(\frac{\Delta\epsilon_{sel}}{\epsilon_{sel}} \right)^2 + \frac{1}{N_{Signal}} + \left(\frac{\Delta L}{L} \right)^2 \right] \tag{4.6}$$

where:

- N_{Signal} is the integral over the red histogram of the mass spectra
- ϵ_{sel} is the selection efficiency
- L is the luminosity

By inserting in the formula the results obtained from the fit in fig. 4.13 and 4.14 we obtain a cross section of 15.08 ± 1.95 fb for the case of the electrons reconstructed with the tracking systems only and a cross section of 16.30 ± 2.31 fb for the case of the electrons reconstructed with the tracking systems and the calorimeter combined.

Conclusions

The International Linear Collider, in the energy range 0.5 - 1 TeV, will be essential to make precise measurements in the region of electroweak symmetry-breaking which will be opened up by the Large Hadron Collider(LHC). The physics topic under study at the ILC require detectors with capabilities far beyond these at LEP or LHC. The ILC machine environment allows for detector designs with superior jet energy, track momentum, and vertex impact parameter resolutions for precision measurements of masses and branching fractions, final states identifiecation, low cross-section signals, new phenomena, and for exploiting the delivered luminosity as much as possible. Detector research and development is still needed to reach these goals. Three ILC detector concepts have emerged in the last few year, the International Large Detector (ILD), the Silicon Detector (SiD) and the 4^{th} Concept. My thesis work has been done within the collaboration of the 4^{th} Concept.

In this work I have discussed in detail the geometry and the perfomances of the central tracker and of the muon spectrometer. I have performed studies of these subdetectors within the 4-th Concept framework with the aid of the ILCRoot software. The obtained results confirm that the proposed CluCou will be able to reach the tracking performance goal, proposed for ILC. The momentum resolution reached can be parametrized as: $\sigma(1/p_T) = 3.9 \times 10^{-5} \oplus 7.9 \times \times 10^{-3}/p_T\ (GeV/c)^{-1}$). These results are comparabile with those obtained in the case of a TPC or of a Silicon tracker. In addition, the results confirm also that the innovative muon system that employs a dual-solenoid magnetic field configuration, allows for a higher precison momentum measurement with rispect to the traditional configuration of a iron yoke flux return:

$$\sigma(1/p_t) = 1.6 \times 10^{-3} \oplus 4 \cdot 10^{-2}$$

A last I conclude describing in detail the physics analysis of the Higgs breemsstrahlung production process, with the identification of the Z in pairs of charged leptons. The values of the calculated cross section are consistent with those simulated.

Bibliography

[1] S.LGlashow,Nul.Phys.2(1961)579.SWeinberg,Phys.Rev.Let.19 (1967)1264.A.SalmandJ.C.Ward,Phys.Let.13(1964)168.

[2] R.D. Field: Perturbative QCD (Addison–Wesley, Redwood City, 1989); F.J. Yndurain: The Theory of Quark and Gluon Interactions (Springer–Verlag, Belin, 1993).

[3] for reviews, see:
E.S. Abers and B.W. Lee: Phys. Rev. **9** (1973) 1;
M.A.B. Beg and A. Sirlin: Phys. Rep. **88** (1982) 1;
P. Langacker: Phys. Rep. **72** (1981) 185;
P. Langacker and J. Erler: Phys. Rev. **D50** (1994) 1304.

[4] P.W.Higgs,Phys.Let.12(1964)132.PW.Higgs,Phys.Rev.145(196) 156.F Englertand R.Brout,Phys.Rev.Let.13(1964)321.G.S.Guralnik,C.R.Hagen and T.W.B. Kible,Phys.Rev.Let.13(1964)58.

[5] D.J. Gross and F. Wilczek: Phys. Rev. Lett. 30, 1343 (1973).

[6] H.D. Politzer: Phys. Rev. Lett. 30, 1346 (1973).

[7] PartileDatGroup,ReviwofParticleProperties",EuropeanPhys.J. C3,2004.

[8] Zeroth-Order Design Report for the Next Linear Collider LBNL-PUB-5424, SLAC Report 474, May 1996.

[9] I. Watanabe et al.: JLC Design Study: KEK Report 97-17 April 1997.

[10] R. Brinkmann et al.: Conceptual Design of a 500 GeV Electron Positron Linear Collider with Integrated X-Ray Laser Facility DESY 97-048, ECFA-97-182: Nuclear Instruments and Methods in Physics Research **A406** (1998) 13.

[11] Referebce Desgne Report Accelerator, Intenational Linear Collider.

[12] Referebce Desgne Report, Physics Studies, Intenational Linear Collider.

[13] ILD Letter of Intent

[14] SiD Letter of Intent

[15] 4th Letter of Intent

[16] A. Khanov: The CMS tracker performance: Nuclear Instruments and Methods in Physics Research **A446** (2000) 338-345.

[17] The KLOE drift chamber: Nuclear Instruments and Methods in Physics Research **A494** (2002) 163-172.

[18] http://fisica.unisalento.it/ danieleb/IlcRoot

[19] http://root.cern.ch

[20] http://aliceinfo.cern.ch/Offline

[21] http://root.cern.ch/drupal/content/vmc

[22] Brun.R et al.:GEANT3:user's guide Geant3.11. CERN Geneve 1987

[23] http://geant4.web.cern.ch/geant4

[24] http://fluka.org

[25] Kalman, R.E. (1960). A new approach to linear filtering and prediction problems Journal of Basic Engineering 82 (1): 3545. http://www.elo.utfsm.cl/ ipd481/Papers%20varios/kalman1960.pdf. Retrieved on 2008-05-03;Kalman, R.E.; Bucy, R.S. (1961). New Results in Linear Filtering and Prediction Theory

[26] http://aliceinfo.cern.ch/Offline/Activities/Reconstruction

[27] F.Grancagnolo: From MARK3 to superB and ILC:Nuclear Instruments and Methods in Physics Research A 579 (2007) 557561

[28] Particle Data Group: Review of Particle Physics: Physics Letters **B 592** (2004) 1-1109.

[29] F. Gancagnolo et alt: A COMOS high speed front end for cluster counting techniques in ionizaion detectors.

[30] R. Perrino a,, A. Baschirotto b,a, G. Chiodini a, PM. Panareo b,a, S. Spagnolo c,a, G. Tassielli c,a:Cluster counting drift chamber as high precision tracker for ILC experiments:Nuclear Instruments and Methods in Physics Research A 598 (2009) 98101

[31] http:://garfield.web.cern.ch/garfield/

[32] S.F. Biagi: Nuclear Instruments and Methods in Physics Research **A421** (1999) 234-240.
http://consult.cern.ch/writeup/magboltz/

[33] Particle Data Group: Review of Particle Physics: Physics Letters **B** **592** (2004) 1-1109.

[34] K.Ito et alt : ZH Recoil Mass and Cross Section Analysis at ILD